# Dynamics of Molecular Gas in the Central Region of the Quasar I Zwicky 1

(article starts on next page)

CrossMark

# Dynamics of Molecular Gas in the Central Region of the Quasar I Zwicky 1

Qinyue Fei[1,2] , Ran Wang[1,2] , Juan Molina[3] , Jinyi Shangguan[4] , Luis C. Ho[1,2] , Franz E. Bauer[5,6,7] , and
Ezequiel Treister[5]

[1] Kavli Institute for Astronomy and Astrophysics, Peking University, Beijing 100871, People's Republic of China; rwangkiaa@pku.edu.cn
[2] Department of Astronomy, School of Physics, Peking University, Beijing 100871, People's Republic of China
[3] Department of Space, Earth and Environment, Chalmers University of Technology, Onsala Space Observatory, SE-439 92 Onsala, Sweden
[4] Max-Planck-Institut für Extraterrestrische Physik (MPE), Giessenbachstr., D-85748 Garching, Germany
[5] Instituto de Astrofísica and Centro de Astroingeniería, Facultad de Física, Pontificia Universidad Católica de Chile, Casilla 306, Santiago 22, Chile
[6] Millennium Institute of Astrophysics (MAS), Nuncio Monseñor Sótero Sanz 100, Providencia, Santiago, Chile
[7] Space Science Institute, 4750 Walnut Street, Suite 205, Boulder, CO-80301, USA

## Abstract

We present a study of the molecular gas distribution and kinematics in the cicumnuclear region (radii $\lesssim 2$ kpc) of the $z \approx 0.061$ quasar I Zwicky 1 using a collection of available Atacama Large Millimeter/submillimeter Array observations of the carbon monoxide (CO) emission. With an angular resolution of $\sim 0\rlap{.}''36$ (corresponding to $\sim 400$ pc), the host-galaxy substructures including the nuclear molecular gas disk, spiral arms, and a compact bar-like component are resolved. We analyzed the gas kinematics based on the CO image cube and obtained the rotation curve and radial distribution of velocity dispersion. The velocity dispersion is about 30 km s$^{-1}$ in the outer CO disk region and rises up to $\gtrsim 100$ km s$^{-1}$ at radius $\lesssim 1$ kpc, suggesting that the central region of the disk is dynamically hot. We constrain the CO-to-H$_2$ conversion factor, $\alpha_{CO}$, by modeling the cold gas disk dynamics. We find that, with prior knowledge about the stellar and dark matter components, the $\alpha_{CO}$ value in the circumnuclear region of this quasar host galaxy is $1.55^{+0.47}_{-0.49}$ $M_\odot$(K km s$^{-1}$ pc$^2$)$^{-1}$, which is between the value reported in ultraluminous infrared galaxies and in the Milky Way. The central 1 kpc region of this quasar host galaxy has significant star formation activity, which can be identified as a nuclear starburst. We further investigate the high-velocity dispersion in the central region. We find that the interstellar medium (ISM) turbulent pressure derived from the gas velocity dispersion is in equilibrium with the weight of the ISM. This argues against extra power from active galactic nuclei feedback that significantly affects the kinematics of the cold molecular gas.

*Unified Astronomy Thesaurus concepts:* AGN host galaxies (2017); Quasars (1319); Galaxy kinematics (602); Galaxy dynamics (591); Molecular gas (1073)

## 1. Introduction

The scaling relationships between supermassive black holes (SMBHs) and their host galaxies suggest that their early evolutionary progress are tightly coupled (e.g., Magorrian et al. 1998; Ferrarese & Merritt 2000; Gebhardt et al. 2000; Kormendy & Ho 2013). Active galactic nuclei (AGNs) represent the most active phase of the coevolution of SMBHs and their host galaxies (Schawinski et al. 2007; Feruglio et al. 2010; King 2010; Rupke & Veilleux 2011; Fabian 2012; Cicone et al. 2014; Fiore et al. 2017; Fluetsch et al. 2019). Cold molecular gas provides fuel for both star formation and SMBH growth (Carilli & Walter 2013; Vito et al. 2014). Studying the distribution and kinematics of the molecular gas is therefore crucial for understanding the physical process involved in the coevolution between SMBHs and their host galaxies (Sanders et al. 1991; Feruglio et al. 2010; Sturm et al. 2011).

The low-order rotational transitions of carbon monoxide (CO) are the most common tracer for studies (e.g., Barvainis et al. 1989; Carilli & Walter 2013; Bolatto et al. 2017; Alonso-Herrero et al. 2018; Tan et al. 2019; Molina et al. 2021; Yajima et al. 2021). Massive molecular outflows reported in previous CO observations of AGN host galaxies have been considered as evidence of

negative AGN feedback, which expels gas and dust from the host galaxy (Haan et al. 2009; Feruglio et al. 2010; Cicone et al. 2014; Morganti et al. 2015). However, recent studies with large samples of optically selected quasars suggest that their host galaxies are falling on, and even above, the main sequence of star-forming galaxies, with the host-galaxy star formation rate (SFR) and SMBH accretion rate being tightly correlated (e.g., Mullaney et al. 2012; Chen et al. 2013; Lanzuisi et al. 2017; Zhuang et al. 2021). From an observational point of view, the impact of AGN feedback on host-galaxy evolution is still under debate, and it is necessary to study the physical processes embedded in AGN host galaxies that govern the coevolution between SMBHs and host galaxies.

Quasars, as the most luminous population of AGNs, are ideal targets for studying the impact of AGN feedback. Shangguan et al. (2020a) observed the CO(2–1) line emission from a sample of 23 $z < 0.1$ Palomar–Green (PG; Schmidt & Green 1983) quasars using the Atacama Compact (Morita) Array (ACA). Molina et al. (2021) provided follow-up Atacama Large Millimeter/submillimeter Array (ALMA) observations of six PG quasars at $\sim$kiloparsec-scale resolution to study the distribution and kinematics of molecular gas in their host galaxies. Their results suggest that quasar hosts and inactive star-forming galaxies have similar gas fractions (Shangguan et al. 2020a) but are more centrally concentrated (Molina et al. 2021); luminous quasars do not efficiently remove cold gas from the host galaxy.

Accurate measurements of the cold gas mass are key to understand the interstellar medium (ISM) evolution in quasar

**Table 1**
ALMA CO(2–1) Observations of I Zw 1

| Project Code | Date of Observation | Observational Band | Configuration | Antenna Number | On-target Time (s) | References |
|---|---|---|---|---|---|---|
| (1) | (2) | (3) | (4) | (5) | (6) | (7) |
| 2017.1.00297.S | Nov. 2017 | Band 6 | ACA | 11 | 8991 | Shangguan et al. (2020a) |
| 2018.1.00006.S | Nov. 2018 | Band 6 | C43–5 | 44 | 699 | Molina et al. (2021) |
| 2018.1.00699.S | Oct. 2018 | Band 6 | C43–5 | 45 | 2992 | Lamperti et al. (2022) |

**Note.** (1) The project code of ALMA observations. (2) The date of ALMA observations. (3) The ALMA band used during the observation. (4) The configuration of ALMA during the observation. (5) The number of antennas that are used during the observation. (6) The total on-target time of observation. (7) Papers that first report the observation.

host galaxies. The molecular gas masses are mainly measured by using the line luminosities of the low-$J$ CO transitions based on assumptions of the CO(1–0) luminosity-to-mass conversion factor, $\alpha_{CO}$, i.e., $M_{H_2} = \alpha_{CO} L'_{CO(1-0)}$. A Millky Way–like value of 3.1 (Sandstrom et al. 2013) is usually assumed for local Seyferts and quasars that are hosted in spiral galaxies (Evans et al. 2006; Shangguan et al. 2020a; Koss et al. 2021), while the ultraluminous infrared galaxy (ULIRG)-like value of $\alpha_{CO} = 0.8\, M_\odot(\mathrm{K\ km\ s^{-1}\ pc^2})^{-1}$(Downes & Solomon 1998) is also considered for AGNs that are hosted in starburst systems (Xia et al. 2012). Studies of star-forming galaxies from local to high-$z$ suggest that the $\alpha_{CO}$ factor varies over a wide range (Solomon et al. 1987; Lombardi et al. 2006; Narayanan et al. 2011; Papadopoulos et al. 2012; Sandstrom et al. 2013) and depends on the metallicity of the ISM (Israel 1997; Wolfire et al. 2010; Leroy et al. 2011). However, there are as yet few direct measurements of $\alpha_{CO}$ in quasar host galaxies (Shangguan et al. 2020a).

High-resolution molecular CO line imaging with ALMA opens a unique opportunity to measure the gas dynamics in nearby quasar host galaxies (e.g., Tan et al. 2019). The rotation curve traced by the CO line velocity field constrains the dynamical mass of the host galaxy, allowing a detailed study of the mass budget from the gas and stellar content and providing an independent way to measure the $\alpha_{CO}$ factor. In this work, we present a case study of the quasar I Zwicky 1 (hereafter I Zw 1). The CO(2–1) emission from its host galaxy was observed by ALMA at $\sim$400 pc scale, the highest spatial resolution (by a factor of $\sim$2–3) among the six objects presented in Molina et al. (2021), which allows us to resolve the gas content in the central few kiloparsecs region. The high-resolution data allows the possibility of dynamical analysis, which is widely used in investigating the accurate mass-to-light ratio in galaxies (e.g., de Blok et al. 2008).

I Zw 1 possesses one of the most complete sets of multi-wavelength spectral energy distribution (SED) data coverage (Phillips 1976; Barvainis & Antonucci 1989; Gallo et al. 2004; Bruhweiler & Verner 2008; Silva et al. 2018; Lyu et al. 2019). Spectroscopic observations indicate that it is a narrow-line Seyfert 1 system with $\mathrm{FWHM}_{H\beta} = 1400\ \mathrm{km\ s^{-1}}$ (Osterbrock 1977), and a black hole mass of $9.30^{+1.26}_{-1.38} \times 10^6 M_\odot$ given by reverberation mapping (Huang et al. 2019). With a bolometric luminosity of $L_{bol} = 3 \times 10^{45}\ \mathrm{erg\ s^{-1}}$, I Zw 1 is quantified as a super-Eddington source with $\lambda_{Edd} = 2.58$. Long-term X-ray monitoring indicates the existence of an ultrafast outflow in the nucleus of I Zw 1 (Ding et al. 2022). Detailed morphological analysis based on Hubble Space Telescope (HST) $0''\!.1$ resolution imaging showed a prominent pseudo-

bulge (Sérsic index $n \approx 1.69$, effective radius $r_e \approx 1.6$ kpc), and a relatively faint and extended disk (Zhao et al. 2021). The pseudo-bulge implies a black hole to bulge mass of $\sim 10^{-4}$, smaller than that of classical bulges and elliptical galaxies by a factor of 50 (Huang et al. 2019). The SED decomposition analysis yields a far-infrared (FIR) luminosity of $\log L_{FIR}/L_\odot = 11.94 \pm 0.30$ (Shangguan et al. 2018), in the range of luminous infrared galaxies (LIRGs). The star formation activity distribution was confirmed with newly developed integrated field unit (IFU) observations (Perna et al. 2021; Lamperti et al. 2022; Molina et al. 2022). The significant star formation activity has also been confirmed by a combination of optical and submillimeter observations (Molina et al. 2023). Previous IRAM and ALMA observations have already suggested that I Zw 1 has a rich molecular gas reservoir, mainly concentrated in its circumnuclear zone (Barvainis et al. 1989; Eckart et al. 1994; Schinnerer et al. 1998; Tan et al. 2019).

This paper is organized as follows. In Section 2 we present the available ALMA archival data of CO(1–0) and CO(2–1) observations and describe the data reduction. In Section 3 we model the molecular gas distribution and kinematics. In Section 4, we model the gas dynamics and estimate the mass of each component, with prior knowledge of stellar distribution and dark matter halo properties. In Section 5 we discuss the CO emission-line ratios and the SFR surface densities, and investigate whether we detect significant AGN feedback. We summarize in Section 6. For standard cosmological parameters of $\Omega_m = 0.308$, $\Omega_\Lambda = 0.692$, and $H_0 = 67.8\ \mathrm{km\ s^{-1}\ Mpc^{-1}}$ (Planck Collaboration et al. 2016), a redshift of $z = 0.06115$ corresponds to a luminosity distance of 283 Mpc.

## 2. CO Data of I Zw 1

We collect available observations of the CO(2–1) line emission of I Zw 1 from the ALMA archive. The final data are combined from three ALMA programs, 2017.1.00297.S, 2018.1.00006.S (PI: Franz Bauer), and 2018.1.00699.S (PI: Pereira Santaella; Shangguan et al. 2020a; Molina et al. 2021; Lamperti et al. 2022). The first observation is our ACA survey, with 2.5 hr on-source integration time and an angular resolution of $7''$ (Shangguan et al. 2020a). The second observation is our follow-up high-angular-resolution observation, with about 11 minutes on-source time and an angular resolution of $0''\!.4$ (Molina et al. 2021). The third observation is a part of the Physics of ULIRGs with MUSE and ALMA (PUMA; Lamperti et al. 2022) project, with 50 minutes on-source time and an angular resolution of $0''\!.3$. We list the details of these observations in Table 1.
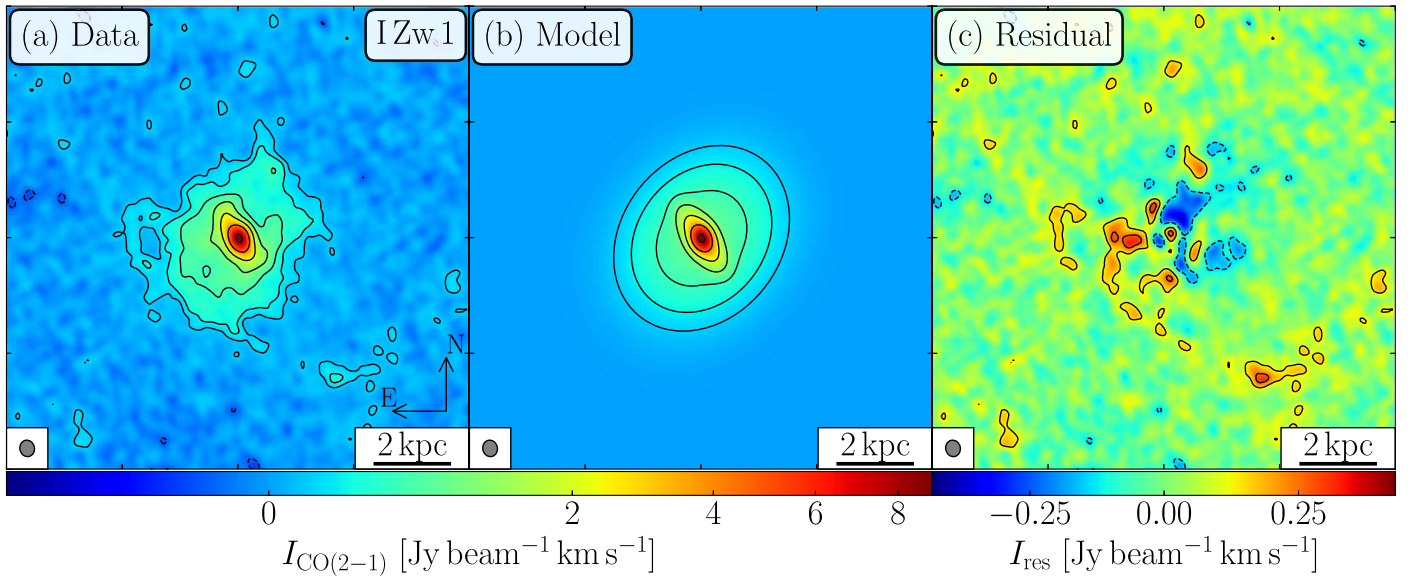
**Figure 1.** Comparison between the observed and modeled intensity maps of the CO(2–1) line emission. Contour levels in each panel correspond to $[-1, 1, 2, 4, 8, 16, 32] \times 3\sigma$, where $\sigma$ is the rms, with the value of 0.043 Jy beam$^{-1}$ km s$^{-1}$. Panels (a) and (b) represent the velocity-integrated map of the data and the model, respectively. Panel (c) represents the residuals between the data and the model. The north and east directions are shown as arrows at the lower-right corner in panel (a). The synthesized beam ($0''36 \times 0''32$) is plotted at the bottom-left corner of each panel.

We use the Common Astronomy Software Application (CASA) version 5.6.1 (McMullin et al. 2007) to reduce the ALMA observation data. All of these observations are concatenated with the CASA task `concat`. The continuum data are fitted and subtracted with the CASA task `uvcont-sub`. We then imaged and cleaned the line data cube and continuum data with Briggs weighting (robustness parameter = 0.5) and a stop threshold 2.5 times the rms of the off-source channels. For the CO(2–1) emission line we set a channel resolution of 7.812 MHz, which corresponds to $\sim$11 km s$^{-1}$ at $z = 0.061$. We set gridder = mosaic during `tclean`, and employ the `auto-multithresh` masking procedure (McMullin et al. 2007). We set the noise, sidelobe, and low-noise thresholds as 4.25, 2.0, and 1.5 as recommended by CASA guidelines.[8] The other additional parameters were not modified. Finally, we obtain a CO(2–1) data cube with a synthesized beam size of $0''36 \times 0''32$, and a typical channel rms noise of 0.28 mJy beam$^{-1}$. We derive the velocity-integrated flux map, intensity-weighted velocity, and velocity dispersion maps using the CASA task `immoments`. The beam size of the 1.3 mm continuum is $0''31 \times 0''28$, and the rms of the continuum map is 0.012 mJy beam$^{-1}$.

We also investigate the surface density distribution of the CO(1–0) emission line, in order to image the CO(2–1)/CO(1–0) emission-line ratio of this target. We build the ALMA CO(1–0) data, which is adapted from the ALMA program 2015.1.01147.S (Tan et al. 2019). We reduce the data following the procedure described previously. The beam size of the CO(1–0) data is $0''62 \times 0''57$.

### 3. Results and Analysis

#### 3.1. Distribution of the Molecular Gas

We present the velocity-integrated intensity map in Figure 1(a). The CO(2–1) line emission in I Zw 1 traces a disk with a diameter of $\sim$5 kpc, which is consistent with the source

size of the CO(1–0) line emission (Tan et al. 2019). In Figure 1(a), we note that the central contours (above $24\sigma$) are elongated along the northeast–southwest direction while the outer, lower-surface-brightness region has a different major axis position angle. This indicates that the molecular gas disk can be described morphologically by two components, one extremely compact bar-like structure, that extends up to $\sim$ 1kpc with a position angle of $\sim$30°, and a well-resolved extended circumnuclear disk (CND). Such elongated structure could also be a massive bipolar gas outflow; however, further kinematic analysis does not show evidence of any noncircular motions (Section 3.2). The large intensity gradient in the nucleus also implies that the CO emission may also exhibit a central compact core component unresolved by ALMA.

The complex molecular gas distribution described above can be well described by fitting the CO(2–1) line-intensity map with three components: two Sérsic (Sérsic 1963) components for the extended emission (Equation (1)) and one Gaussian component for the unresolved core (Equation (2)):

$$I_s(r) = I_e \exp\left\{-b_n\left[\left(\frac{r}{r_e}\right)^{1/n} - 1\right]\right\}, \qquad (1)$$

$$I_g(r) = I_G \exp\left\{-\frac{r^2}{2\sigma^2}\right\}, \qquad (2)$$

where $I_e$ is the surface brightness measured at $r_e$, the effective radius, $n$ is the Sérsic index, and $b_n$ is the numerical coefficient that ensures $r_e$ corresponds to the half-light radius (Sérsic 1963). We use these two Sérsic profiles to describe the bar-like structure and disk component, respectively, and use the Gaussian profile to describe the central compact core. We built this three-component model with Astropy (Astropy Collaboration et al. 2013), which is then convolved with the observation synthesized beam to produce the model of the observed line-intensity map. The three-component model contains 16 free parameters, including $I_e$, $r_e$, $n$, minor-to-major

**Table 2**
Fitting Parameters of CO(2–1) Intensity Map

| | $I_e$ (Jy beam$^{-1}$ km s$^{-1}$) (1) | $R_e$ ('') (2) | $n$ (3) | $b/a$ (4) | $\phi_s$ (°) (5) |
|---|---|---|---|---|---|
| CND | $0.44^{+0.01}_{-0.01}$ | $1.30^{+0.01}_{-0.01}$ | $0.48^{+0.01}_{-0.01}$ | $0.80^{+0.01}_{-0.01}$ | $141.90^{+0.40}_{-0.40}$ |
| Bar | $2.37^{+0.05}_{-0.05}$ | $0.50^{+0.01}_{-0.01}$ | $0.30^{+0.20}_{-0.20}$ | $0.32^{+0.01}_{-0.01}$ | $33.65^{+0.11}_{-0.11}$ |

| | $I_G$ (Jy beam$^{-1}$ km s$^{-1}$) (6) | FWHM$_{maj}$ (mas) (7) | FWHM$_{min}$ (mas) (8) | $\phi_G$ (°) (9) |
|---|---|---|---|---|
| Core | $29.90^{+0.73}_{-0.70}$ | $221.35^{+0.01}_{-0.01}$ | $122.45^{+0.01}_{-0.01}$ | $16.59^{+1.36}_{-1.56}$ |

**Note.** (1) Intensity at effective radius. (2) Effective radius. (3) Sérsic index. (4) The minor-to-major axis ratio. (5) Position angle of the major axis. North = 0°, east = 90°. (6) Amplitude of the Gaussian function. (7) and (8) FWHM of the major and minor axes. (9) The position angle of the major axis of the Gaussian component.

axis ratio ($b/a$), position angle ($\phi_s$) for each of the two Sérsic components, Gaussian amplitude ($I_G$), FWHM along the major and minor axes (FWHM$_x$, FWHM$_y$), position angle of the major axis ($\phi_G$) for the Gaussian component, and the center location ($x_0$, $y_0$) that is shared with all three components.

To find the best-fitting model we use the Python package `emcee` (Foreman-Mackey et al. 2013). The `emcee` package implements the affine-invariant ensemble sampler for the Markov Chain Monte Carlo (MCMC) sampling method to sample the posterior probability distribution function. We optimize the log-likelihood function:

$$\log \mathcal{L} \equiv -\frac{1}{2}\sum_i^N \left[ \frac{(z_i - z_i^m)^2}{\sigma_i^2} + \ln(2\pi\sigma_i^2) \right], \qquad (3)$$

where $z_i$ denotes the surface brightness at each pixel, $\sigma_i$ is the $1\sigma$ noise, and $z_i^m$ corresponds to the model value at the same pixel. The best-fitting model along with residuals are shown in Figure 1, and the best-fitting parameters are presented in Table 2.

With the assumption that the CND and stellar disk are coplanar, we estimate the inclination angle of the disk following the formula in Hubble (1926):

$$\cos^2 i = \frac{(b/a)^2 - q_0^2}{1 - q_0^2}, \qquad (4)$$

where $q_0$ is the intrinsic galaxy thickness, and $b/a$ is the minor-to-major axis of the CND. We assume $q_0 = 0.14$ for the molecular gas disk, which is similar to that reported for edge-on galaxies at low redshifts (Mosenkov et al. 2015). We obtain a host-galaxy inclination $i = 38°$.

From Figure 1, we can see that our model presents a reasonable description of the gas distribution in the circum-nuclear scale. The residuals are likely to be produced by partially resolved out spiral arms, as can be seen at the southwest edge.

### 3.2. $^{3D}$Barolo Fitting

The intensity-weighted velocity and velocity dispersion maps of the CO(2–1) line emission are shown in panels (a) and panel (d) in Figure 2. As discussed in Molina et al. (2021), the gas velocity field is dominated by circular rotation. The velocity dispersion in the outer region is almost constant

($\sim$30 km s$^{-1}$) with small variations along the radius, while in the inner 1 kpc region the velocity dispersion rises up to 100 km s$^{-1}$.

Assuming that the noncircular motions are negligible, we fit the velocity field with a tilted-ring model (Rogstad et al. 1974). The rotating disk is decomposed into a series of thin rings, and the kinematic properties of each ring can be described by seven parameters:

1. ($x_0$, $y_0$): the sky coordinates of the ring center.
2. $V_{sys}$: the systematic velocity of the center of the ring related to the observer.
3. $V_{rot}(R)$: the rotation velocity of the ring.
4. $\sigma$: the velocity dispersion of the ring.
5. $\phi(R)$: the position angle of the kinematic major axis on the receding half of the galaxy, with respect to the north direction.
6. $i(R)$: the inclination angle between the normal to the ring and the line of sight; Inc. = 0° represents a face-on disk.
7. $z_0$: the scale height of the gas layer.

The line-of-sight velocity field [$V_{los}(x, y)$] that we observed is related to the above parameters:

$$V_{los}(x, y) = V_{sys} + V_{rot}(R)\sin i(R)\cos\theta$$
$$\cos\theta = \frac{-(x - x_0)\sin\phi + (y - y_0)\cos\phi}{R},$$

where $R$ is the radius of each ring.

In order to obtain the intrinsic kinematics of the molecular gas in this galaxy, we model the ALMA data cube using 3D-Based Analysis of Rotating Objects from Line Observations ($^{3D}$Barolo, version 1.6; Di Teodoro & Fraternali 2015). $^{3D}$Barolo fits the three dimensions of the data cubes with a tilted-ring model. By directly modeling the data cube instead of the 2D velocity map, it fully accounts for the beam-smearing effect, providing a reasonable model of the intrinsic circular velocity and velocity dispersion field for circular rotating systems (see Di Teodoro & Fraternali 2015 for more details).

We fit the gas kinematics with $^{3D}$Barolo in two steps following the procedure described in Alonso-Herrero et al. (2018), but with some revisions. In the first step, we set the galaxy center ($x_0$, $y_0$), systematic velocity $V_{sys}$, rotation velocity $V_{rot}$, velocity dispersion $\sigma$, position angle $\phi$, inclination $i$, and disk height $z_0$ parameters to be free. We adopt a ring width of $0\rlap{.}''1$ in the fitting, roughly one-third of the beam size. Initial
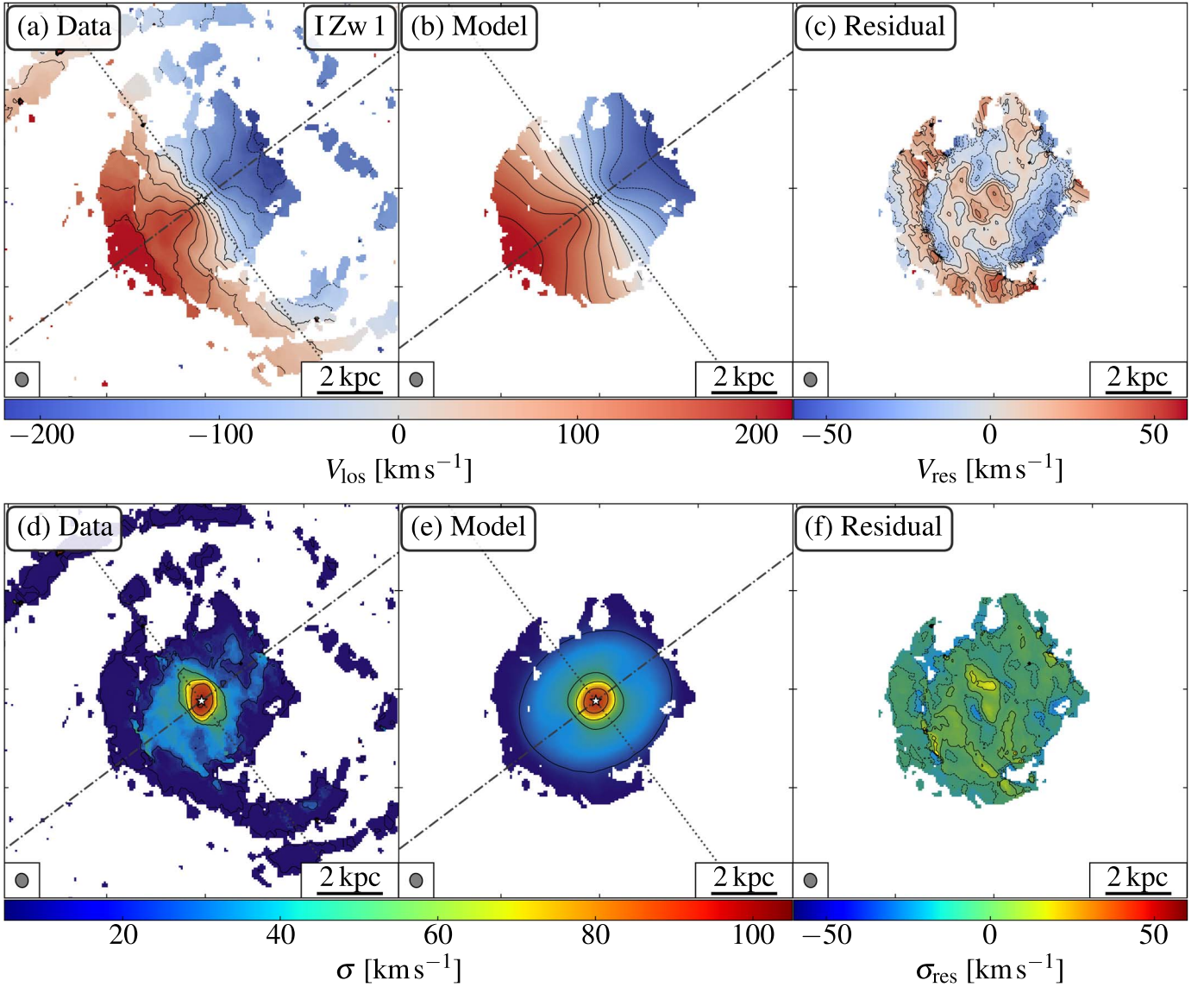
**Figure 2.** The results of $^{3D}$Barolo fitting. Panels (a) and (b) represent the line-of-sight velocity map of the CO(2–1) data and the best-fitting model given by $^{3D}$Barolo. Panel (c) represents the residual between the observation and the model. Panels (d) and (e) represent the velocity dispersion of the data and the $^{3D}$Barolo model. Panel (f) represents the residual of the velocity dispersion map. Contours in panels (a) and (b) start from $-200$ km s$^{-1}$ and are in steps of 40 km s$^{-1}$. Contours in panels (d) and (e) are from 5 km s$^{-1}$ and in steps of 40 km s$^{-1}$. Contours in residual maps range from $-50$ to 50 km s$^{-1}$ and are in steps of 20 km s$^{-1}$. The white star in each subpanel indicates the kinematics center. The dashed–dotted and dotted lines represent the major and minor kinematic axes.

guesses for the position angle and inclination are adopted from the morphological model results ($\phi = 142°$ and $i = 38°$; Section 3.1). Initial guesses for the kinematic center are set to be the same as the morphological center. We find that the output kinematic centers of each ring from this initial center are almost constant along the CND, in radii between 0.8 and 2.1 kpc. However, the fitting kinematic centers of the inner and outer rings show large scatter and uncertainties, which is possibly due to the limited resolution, poor sampling, and complex dynamics caused by the compact, central bar-like structure and possible companion interaction in the outer region (Shangguan et al. 2020a). Other fitting parameters, such as $V_{sys}$, are almost constant within the CND. During the second fitting step, we fix the kinematic center and systematic velocity to the mean values over CND scale that are obtained from the first fitting step, then to fit the rotation velocities, velocity dispersions, position angles, and inclination angles for each ring. The $^{3D}$Barolo best-fitting results are shown in Figure 3.

The 3D model successfully describes the CND cold gas kinematics, with rms model residuals $\approx 20$ km s$^{-1}$ and $\approx 10$ km s$^{-1}$ for the rotation velocity and velocity dispersion fields, respectively. The latter is comparable to the velocity resolution of the observation.

### 3.3. Global Kinematics

In panels (a) and (b) of Figure 3 we show the velocity and angle radial profiles derived by $^{3D}$Barolo. The rotation velocity rises to the flattened part at $\sim 0.8$ kpc, with a value of $\sim 270$ km s$^{-1}$, and slightly increases toward a larger radius in the spiral arm region ($r > 2.1$ kpc). In this region, the velocity dispersion is $\sim 30$ km s$^{-1}$, which indicates a cold gas disk with $V/\sigma \approx 9$.

The velocity dispersion profile increases from 30 km s$^{-1}$ at $\sim 0.8$ kpc to 100 km s$^{-1}$ at $\sim 0.3$ kpc. A similar high central velocity dispersion was also reported in previous work Molina
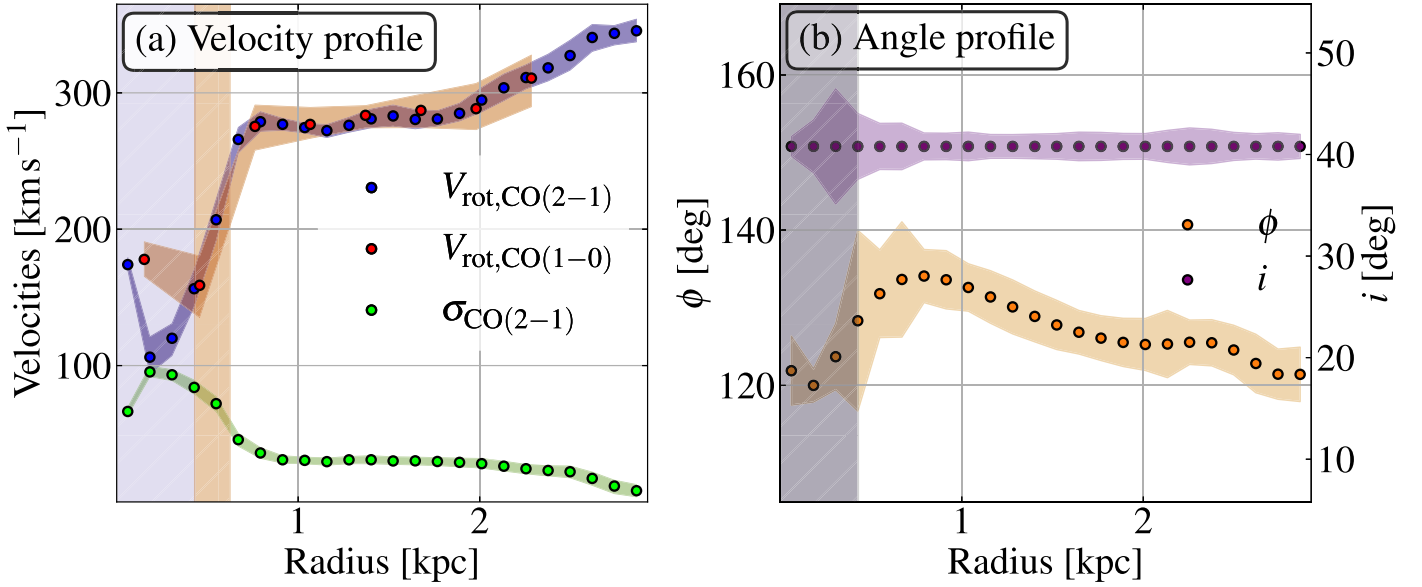
**Figure 3.** The rotation velocity, velocity dispersion, inclination angle, and kinematic position angle derived from $^{3D}$Barolo fitting to the CO(2–1) data. Panel (a) represents the rotation velocities (blue points) and velocity dispersions (green points) as a function of radius. Red points represent the rotation velocities extracted from the CO(1–0) data at a resolution of $\sim$600 pc for comparison. Panel (b) represents the position angle of the kinematic major axis (purple points) and the inclination angle (orange points) as a function of radius. The uncertainties of parameters are shown as colored shades. The blue and red vertical shaded region represents the beam size of the observation for the CO(2–1) and CO(1–0) observations.

et al. (2021), and was found in other galaxies (e.g., Romeo & Fathi 2015). This enhanced velocity dispersion in the central region is not likely to be spurious due to the beam-smearing effect as $^{3D}$Barolo is designed to take this into account (Di Teodoro & Fraternali 2015). To further check this, we build a mock disk model, adopting an intrinsic rotation curve of I Zw 1 and a constant velocity dispersion of $\sigma = 30$ km s$^{-1}$ at all radii. We set the inclination angle and position angle equal to 41° and 130°, which are the same as those in I Zw 1. We then simulate the ALMA observational data cube in CASA using the `simobserve` task and fit the mock data cube with $^{3D}$Barolo. Through our simulated data, we find that the beam-smearing effect can only increase the velocity dispersion value by a factor of $\sim$1.3, insufficient to account for the observational increase of a factor of $\sim$4. Thus, we conclude that the velocity dispersion is intrinsically high in the center region (see detailed discussion in Appendix A). We investigate the origin of such high-velocity dispersion in Section 5.3.

Naturally, $^{3D}$Barolo poorly fits the data cube in the zones where the inner spiral arms are present, but those regions display significant noncircular motions reflecting the local perturbation of the gravitational potential field. Additional kinematic components may be included for a more accurate model for those regions. Molina et al. (2021) investigated the noncircular motion of the CO(2–1) line velocity field of this object with KINEMETRY (Krajnović et al. 2006), finding that noncircular motions are negligible. However, the compact bar-like structure presented in our morphological analysis could still introduce noncircular components in the velocity field of the very central region ($\lesssim$1 kpc), which requires higher-resolution observations to fully resolve the bar-like structure kinematics.

### 3.4. Continuum

Figure 4 shows the 1.3 mm map of this galaxy. Although the size of the continuum map is more compact than that of the
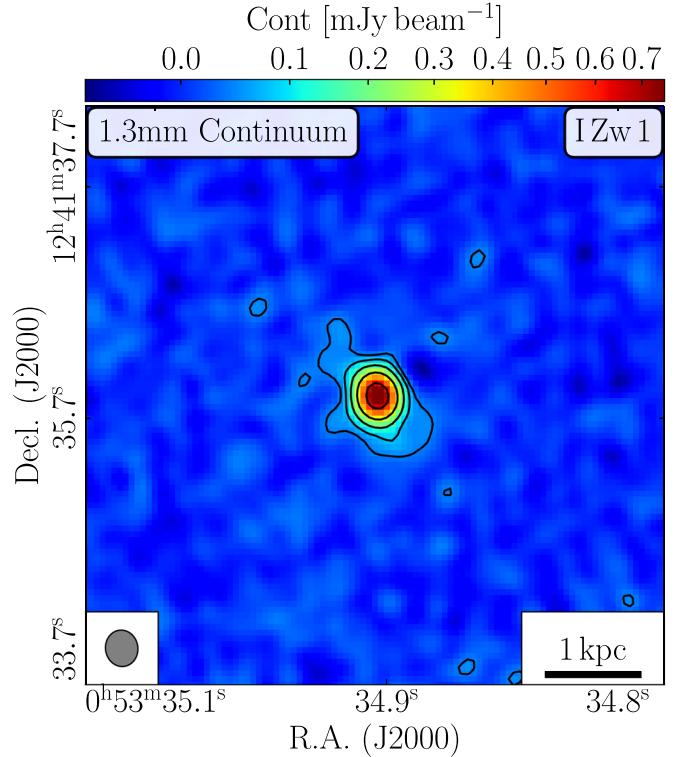


**Figure 4.** The 1.3 mm continuum map of the I Zw 1 host galaxy. The contour levels correspond to $[-1, 1, 2, 4, 8, 16, 32] \times 3\sigma$, where $\sigma = 0.012$ mJy beam$^{-1}$. The synthesized beam ($0''31 \times 0''28$) is plotted at the lower-left corner.

CO(2–1) line-emitting region, we still can see the structure which is elongated in a northeast-to-southwest direction. The continuum source has a position angle similar to that of the molecular bar-like structure. The total flux density within the $3\sigma$ "contour" region is $1.1 \pm 0.1$ mJy, which covers 73% of the continuum flux density obtained from the previous ACA

observation and 34% of the continuum flux density from global FIR SED-fitting prediction (Shangguan et al. 2018, 2020a).

We fit the size of the continuum using the `imfit` task in CASA, which performs synthesized beam deconvolution and 2D Gaussian fitting to the images. The resulting deconvolved FWHM of the major and minor axes sizes are $0\farcs174 \pm 0\farcs014$ and $0\farcs100 \pm 0\farcs017$, corresponding to $(0.21 \pm 0.02) \times (0.02 \pm 0.01)$ kpc$^2$, with a position angle of $23\fdg5 \pm 9\fdg9$.

## 4. Dynamical Modeling and the CO-to-H$_2$ Conversion Factor

The rotation curve modeled with $^{3D}$Barolo provides an independent constraint on the mass distribution within the CO line-emitting region. In this section, we fit the rotation curve with a multicomponent dynamical model to investigate the mass budget of the stellar, molecular gas, and dark matter halo. In particular, with knowledge of the dynamical mass measured with the rotation curve and the stellar mass from HST images (Zhao et al. 2021), we can constrain the mass of the molecular gas and estimate the CO-to-H$_2$ conversion factor, $\alpha_{\rm CO}$.

Here we model the gas dynamics and fit it to the rotation curve derived from $^{3D}$Barolo within the $0.4 \sim 2.1$ kpc radial zone (Figure 3). The inner and outer regions are not considered in the fitting due to the large uncertainties and possible effects from asymmetric structure/spiral arms, discussed in Section 3.3. During the fitting procedure, we assume that the rotation velocity is mainly contributed by four components: the stellar bulge, stellar disk, molecular gas disk, and dark matter halo. We neglect the H I gas component as it is usually much more extended than stars and molecular gas, and thus it only dominates the gas mass on a larger scale (Walter et al. 2008; Wang et al. 2016). We also do not consider the contribution from the SMBH, which has a mass of $9.30^{+1.26}_{-1.38} \times 10^6 \, M_\odot$ (Huang et al. 2019) and has a negligible contribution to the rotation velocity on kiloparsec scales. Thus, the total rotation velocity is calculated as follows:

$$V_{\rm circ,tot}^2 = V_{\rm bulge}^2 + V_{\rm disk}^2 + V_{\rm DM}^2 + V_{\rm gas}^2,$$

where $V_{\rm bulge}$, $V_{\rm disk}$, $V_{\rm DM}$, and $V_{\rm gas}$ are the circular velocities contributed by the stellar bulge, stellar disk, dark matter halo, and molecular gas, respectively.

### 4.1. Circular Velocities

For the spherical stellar bulge component, we adopt the deprojected symmetric 3D model from Prugniel & Simien (1997):

$$\rho(r) = \rho r^{-\alpha} \exp(-b_n r^{1/n}), \qquad (5)$$

where $\alpha$ can be estimated as $\alpha = 1 - 1.188/2n + 0.22/4n^2$ (see Equation (B7) in Prugniel & Simien 1997). A traditional 2D Sérsic profile can be well reproduced by integrating the spatial densities along the line of sight. The circular velocity contributed by the stellar bulge can be written as

$$V_{\rm bulge}(r)^2 = \frac{GM(r)}{r},$$
$$M(r) = M_0 \frac{\gamma[n(3-p), bx^{1/n}]}{\Gamma[n(3-p)]},$$

where $r$ is the spatial radius, and $M_0$ is the total stellar mass of the bulge. $\Gamma$ and $\gamma$ are gamma and incomplete gamma

functions, $x \equiv r/r_e$ is the reduced radius. When the Sérsic index and radius satisfy the relation $0.6 < n < 10$ and $10^{-2} \leqslant r/r_e \leqslant 10^3$, the value of $p$ can be computed as $p = 1.0 - 0.6097/n + 0.05563/n^2$ (Prugniel & Simien 1997). Three parameters are used to describe the bulge mass distribution: the total mass $M_b$, the effective radius $r_{e,b}$, and the Sérsic index $n$.

For the disk component, we use the traditional exponential thin disk model, adopted from Binney & Tremaine (2008):

$$V_{\rm disk}(r)^2 = 4\pi G \Sigma_0 R_d y^2 [I_0(y) K_0(y) - I_1(y) K_1(y)],$$

where $\Sigma_0 = M_d/2\pi r_{e,d}^2$ is the surface density, $R_d = r_{e,d}/1.68$, and $y \equiv r/2R_d$. Here, $M_d$ and $r_{e,d}$ are the stellar disk mass and the disk effective radius. $I_i$ and $K_i$ are Bessel functions. Considering that the main purpose of our study is to constrain the mass component decomposition, we constrain the $r_{e,b}$ and $r_{e,d}$ from Zhao et al. (2021). Both parameters have Gaussian priors, with a typical standard deviation of 0.05. The Sérsic index for the stellar disk is fixed to 1.

For the dark matter component, we adopt a simulation-motivated Navarro–Frenk–White (NFW; Navarro et al. 1996) model, and the circular velocity can be calculated by

$$\left[\frac{V_{\rm DM}(r)}{V_{\rm vir}}\right]^2 = \frac{1}{x} \frac{\ln(1 + cx) - (cx)/(1 + cx)}{\ln(1 + c) - c/(1 + c)},$$

where $x = r/r_{\rm vir}$ is the radius in units of virial radius, $V_{\rm vir}$ is the virial velocity, and $c$ is the halo concentration (see Navarro et al. 1996 for more details). Considering that our rotation curve only traces the nuclear region, where the contribution from dark matter is minor and cannot be well constrained, we let the dark matter parameters satisfy some empirical correlations from numerical simulations. The stellar mass fractions satisfies $-2.3 \leqslant \log(M_*/M_h) \leqslant -1.3$ for halo mass ranges between $10^{11} \, M_\odot$ and $10^{13} \, M_\odot$ (Behroozi et al. 2010). The concentration follows the function $\log c = a + b \log(M/10^{12} h^{-1} M_\odot)$, and we assume an intrinsic standard deviation of 0.1 dex (Dutton & Macciò 2014). Other dark matter profiles (e.g., Burkert 1995) are not considered here as the fitting is not sensitive to different assumptions of dark matter profiles.

We calculate $V_{\rm gas}$ for the molecular gas component following Equation (10) in Noordermeer (2008), which derived the rotation curve for an axisymmetric bulge with arbitrary flattening. In this model, the mass density can be written as $\rho = \rho(m)$, with $m = \sqrt{x^2 + y^2 + (z/q)^2}$, and $q$ is the intrinsic axis ratio of the bulge isodensity surfaces (Noordermeer 2008). The models in Noordermeer (2008) have four parameters: the surface density of the gas $\Sigma_g$, the effective radius $r_{e,g}$, the Sérsic index $n_g$, and the intrinsic axis ratio $q$. Since we know the surface brightness of CO emission from our ALMA observation, we can directly convert the CO line surface brightness to molecular gas surface density with $\alpha_{\rm CO}$. We adopt an intrinsic axis ratio of $q = H/r_e = 0.15$ during fitting, by assuming a scale height of the molecular gas disk $H \sim 150$ pc and $r_e \sim 1$ kpc from previous studies of gas-rich systems (Wilson et al. 2019; Molina et al. 2021). Based on the line ratio distribution from Figure 6, we adopt $R_{21} = 0.9$ for the central region and $R_{21} = 0.6$ for the outer region ($R > 0.8$ kpc) to convert the CO(2–1) line intensity to the CO(1–0) line.

**Table 3**
Constraints and Results of Dynamical Parameters

| | $\log M_b$ $(M_\odot)$ (1) | $r_{e,b}$ (kpc) (2) | $n$ (3) | $\log M_d$ $(M_\odot)$ (4) | $r_{e,d}$ (kpc) (5) | $\log f_*$ (6) | $\log c$ [a] (7) | $\alpha_{CO}$ $M_\odot (\text{K km s}^{-1}\text{pc}^2)^{-1}$ (8) |
|---|---|---|---|---|---|---|---|---|
| Prior | (9.5, 12.5) | $1.62 \pm 0.05$ | $1.69 \pm 0.05$ | (9.1, 12.1) | $10.97 \pm 0.50$ | (−2.25, −1.30) | (0.52, 1.12) | (0, 20) |
| Posterior | $10.70^{+0.08}_{-0.10}$ | $1.61^{+0.05}_{-0.05}$ | $1.70^{+0.05}_{-0.05}$ | $10.46^{+0.60}_{-0.84}$ | $11.00^{+0.49}_{-0.51}$ | $-1.74^{+0.32}_{-0.33}$ | $0.83^{+0.34}_{-0.33}$ | $1.55^{+0.47}_{-0.49}$ |

**Notes.** (1) The stellar bulge mass. (2) The effective radius of the stellar bulge. (3) The Sérsic index of the stellar bulge. (4) The mass of the stellar disk. (5) The effective radius of the stellar disk. (6) The stellar-to-dark matter mass ratio $f_* \equiv M_*/M_h$, where $M_*$ is the total stellar mass and $M_h$ is the dark matter halo mass. (7) The concentration of the dark matter halo. (8) The CO-to-$H_2$ conversion factor. The uniform prior limits of the parameters are denoted as "(lower, upper)." The Gaussian priors of the parameters are denoted as "$\mu \pm \sigma$." In our MCMC fitting, we set Gaussian priors for $r_{e,b}$, $n$, and $r_{e,d}$ from Zhao et al. (2021). We set upper and lower limits for $M_b$, $M_d$, $f_*$, and $c$ from the literature (Behroozi et al. 2010; Dutton & Macciò 2014; Zhao et al. 2021).
[a] Dutton & Macciò (2014) suggested a relationship between dark matter halo concentration and dark matter halo mass from numerical simulations, with an uncertainty of ~0.1 dex. Here we adopt this simulation-driven concentration value $c_{fit}$ as the prior knowledge in our dynamical analysis.

### 4.2. Asymmetric Drift Correction

The ISM pressure gradients can also provide support to the gas against galaxy self-gravity. This effect needs to be considered and corrected for the rotation curve (asymmetric drift correction; Burkert et al. 2010; Lang et al. 2017) as

$$V_{rot}^2 = V_{circ,tot}^2 + \frac{1}{\rho}\frac{d(\rho\sigma^2)}{d\ln r},$$

where $V_{circ}$ is the circular velocity derived from the mass model, $V_{rot}$ is the observed rotation velocity, and the rightmost term models the effect of asymmetric drift, making $V_{rot} < V_{circ}$. In this term, $\sigma$ is the isotropic velocity dispersion, $\rho$ is the gas density, and $r$ is the galactic-to-center radius. Traditionally, $\sigma$ is assumed to be a constant during the application of this asymmetric drift correction (e.g., Burkert et al. 2010), however we find that in this galaxy $\sigma$ is not constant along the radius (Section 3.2), which means that we cannot directly use this formula.

Considering this, we recalculate the asymmetric drift correction with our assumption of vertical hydrostatic equilibrium of the molecular gas:

$$P_{ISM} = \mathcal{W},$$

where $P_{ISM} \propto \rho\sigma^2$ is the ISM turbulent pressure. This assumption is further confirmed in Section 5.3. We find that the asymmetric drift correction can be written as

$$V_{rot}(r)^2 = V_{circ,tot}(r)^2 + \sigma^2\frac{d\ln\Sigma_g}{d\ln r} + \sigma^2\frac{d\ln\Sigma_{tot}}{d\ln r}, \quad (6)$$

where $\Sigma_g$ is the gas surface density and $\Sigma_{tot}$ is the surface density of the total disk, including gas and the stellar component. Since $\sigma$ has been provided by our $^{3D}$Barolo fitting, and $\Sigma_g$ and $\Sigma_{tot}$ can be derived from $\alpha_{CO}$ and stellar mass during the fitting, we can constrain these parameters with our dynamical model. Although $h_g$ remains uncertain, we find the variation of this parameter does not affect the asymmetric drift correction significantly, so we assume a constant value of 150 pc. We also note that when gravity is dominated by gas or stars, Equation (6) reduces to its traditional form in Burkert et al. (2010).

In general, we have eight free parameters in our fitting: the masses of the stellar bulge and stellar disk, the Sérsic index of the stellar bulge, the effective radii of the stellar bulge and the stellar disk, the dark matter halo mass and concentration, and the CO-to-$H_2$ conversion factor.

We use emcee to determine the best-fit values. In order to minimize the free parameters and avoid degeneracy, we set prior constraints following the available stellar galaxy morphology models for the host galaxy, as well as the relation between the dark matter halo and stellar mass content. We set Gaussian priors for the effective radius of the stellar bulge and stellar disk, and the Sérsic index of the bulge following the fitting results and uncertainties from $B$- and $I$-band HST image modeling (Zhao et al. 2021). The prior constraints and posterior derived values are listed in Table 3.

### 4.3. Best-fit Dynamical Modeling and Results

We start the MCMC sampling by using 400 walkers, with 1000 steps after a burn-in of 400 steps. We then adopt the 50th percentile of samples as the best-fit values, and estimate uncertainties using the 16th and 84th percentiles of the samples. The best-fit results and the posterior distribution of bulge mass, disk mass, and $\alpha_{CO}$ are shown as Figure 5.

We find that the geometry parameters (effective radius and Sérsic index) are the same as their prior constraints, which suggests that the rotation curve cannot provide enough information to determine all of the parameters. We still use these prior constraints rather than fix them in order to take into account the uncertainties of these parameters from Zhao et al. (2021). We find that the masses of the stellar bulge and stellar disk are consistent with those in Zhao et al. (2021), while the stellar disk mass has quite large uncertainty. Such large uncertainties are also found in the posterior distribution of the stellar fraction and concentration parameters of the dark matter halo. The large uncertainties imply that they are hardly constrained in our dynamical model; the gravitational potential of the region traced by CO(2–1) is dominated by the stellar bulge and molecular gas. Other components only have minor contributions, and the fitting results are heavily affected by the uncertainties of the stellar bulge and molecular gas masses. We also test the fitting results with different initial setups, and, in most cases, the posterior probability distributions are consistent with each other (see more details in Appendix B).

We derive $\alpha_{CO} = 1.55^{+0.47}_{-0.49}$ $M_\odot (\text{K km s}^{-1} \text{pc}^2)^{-1}$ from our dynamical method. This value is between the Milky Way (MW)–like ($\alpha_{CO} \approx 4.3$ $M_\odot (\text{K km s}^{-1} \text{pc}^2)^{-1}$) and ULIRG-like ($\alpha_{CO} \approx 0.8$ $M_\odot (\text{K km s}^{-1} \text{pc}^2)^{-1}$) values; Downes & Solomon 1998; Bolatto et al. 2013). This value is ~2 times smaller than that in nearby star-forming galaxies (Sandstrom et al. 2013).
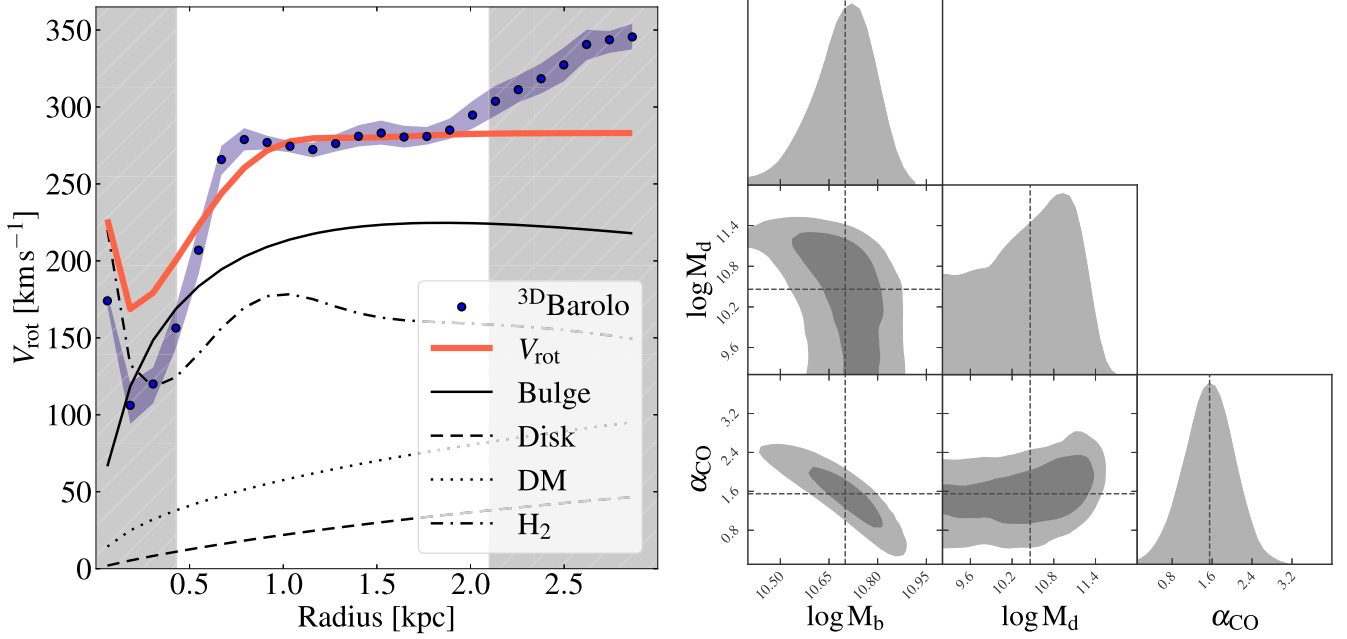
**Figure 5.** Left: derived rotation curve from ³ᴰBarolo and from the best-fitting result. The blue line represents the rotation curve derived from ³ᴰBarolo and its surrounding blue shaded region represents the uncertainties. The black solid line shows the rotation curve of the stellar bulge and the dashed–dotted line shows the rotation curve of the molecular gas. The dashed line shows the rotation curve of the stellar disk. The dotted line shows the rotation curve of dark matter. The thick red solid line represents the result of the best-fit model rotation velocity. The vertical gray shaded region represents the region within the central synthesized beam area in which the data points are not used in the fitting. Right: the posterior distribution of the stellar bulge mass, stellar disk mass, and the CO-to-$H_2$ conversion factor. The vertical and horizontal dashed lines represent the mean value of each parameter, which are adopted as the best-fitting values and are listed in Table 3. The stellar disk mass is poorly constrained, as its contribution is minor in the nuclear region and therefore is heavily degenerate with the stellar bulge component.

The $\alpha_{CO}$ value we derived here is only valid within the ∼2 kpc region of the quasar host galaxy, where the high gas surface density and SFR surface density suggest a nuclear starburst (see Section 5.2). The current CO(2–1) data cannot trace the molecular gas in the extended galactic disk and spiral arm region, where a higher $\alpha_{CO}$ value may remain more appropriate to estimate the molecular gas mass. We also check whether this $\alpha_{CO}$ value is reasonable given some theoretical prescriptions (e.g., Bolatto et al. 2013). Bolatto et al. (2013) indicate that $\alpha_{CO}$ could have large variations depending on metallicity and gas surface density. However, we note that I Zw 1 presents a metallicity of $\log(O/H) = 8.77$ by adopting the $M_* - Z$ relationship obtained for Sloan Digital Sky Survey galaxies with the Pettini & Pagel (2004) calibration (Kewley & Ellison 2008), which is close to solar metallicity. Therefore, we do not expect any significant $\alpha_{CO}$ variation due to high metallicity. We estimate an $\alpha_{CO}$ value of $\sim 1.9\ M_\odot\ (K\ km\ s^{-1}\ pc^2)^{-1}$ by solving the $\alpha_{CO} - \Sigma_{mol}$ relation of Bolatto et al. (2013). This value is consistent with our dynamical $\alpha_{CO}$ value considering the uncertainties.

By adopting this new $\alpha_{CO}$, we estimate a total cold molecular gas mass at a value of $\log M_{H_2}/M_\odot = 9.94^{+0.18}_{-0.31}$, and the gas fraction is $f_{gas} = 0.10^{+0.12}_{-0.08}$. The value of the gas fraction is similar to that in inactive star-forming galaxies and hard-X-ray-selected AGN host galaxies (Shangguan et al. 2020b; Koss et al. 2021), and is smaller than that in local LIRGs by a factor of ∼2 (Larson et al. 2016).

Using our dynamical method, we first investigate the $\alpha_{CO}$ value in this quasar host galaxy, and find that the value of $\alpha_{CO}$ is between that in ULIRGs and in the MW (Bolatto et al. 2013; Molina et al. 2020). In the remaining part of this work, we estimate the molecular gas mass by adopting the median

CO-to-$H_2$ conversion factor value derived from our best dynamical model.

## 5. Discussion

### 5.1. Distribution of the CO(2–1)-to-CO(1–0) Line Ratio

A CO(2–1)-to-CO(1–0) line luminosity ratio of $R_{21} = 0.63 \pm 0.02$ is reported in Shangguan et al. (2020a) based on previous ACA measurements of the total gas content, which is within the typical range for subthermal CO-excited molecular gas in galactic disks ($R_{21} < 0.8$; Leroy et al. 2013; Rosolowsky et al. 2015; Saintonge et al. 2017). Here we report the surface brightness ratio distribution estimated from the resolved ALMA images of CO(2–1) and CO(1–0) that are shown in Section 2. We smooth the CO(2–1) line image with CASA task `imsmooth` to match the angular resolution of the CO(1–0) data. We estimate the surface brightness ratio with `immath` within the region where both signal-to-noise ratios (S/Ns) are larger than 5. The emission-line ratio map is shown in Figure 6.

The line-intensity ratio is close to 1 within the radius of ∼1 kpc in the quasar host galaxy, suggesting that the molecular gas in the central region is optically thick and thermalized. The high $R_{21}$ value in the nuclear region is consistent with the previous result reported by Staguhn et al. (2004) based on Berkeley-Illinois Maryland Association and Plateau de Bu Interferometer observations at a lower angular resolution of ∼0″7 for CO(1–0) and of ∼0″9 for CO(2–1) data. A similar emission-line ratio distribution with a higher value toward the center is commonly found in nearby spiral galaxies (Braine & Combes 1992; den Brok et al. 2021; Yajima et al. 2021), local infrared luminous galaxies (Papadopoulos et al. 2012), and
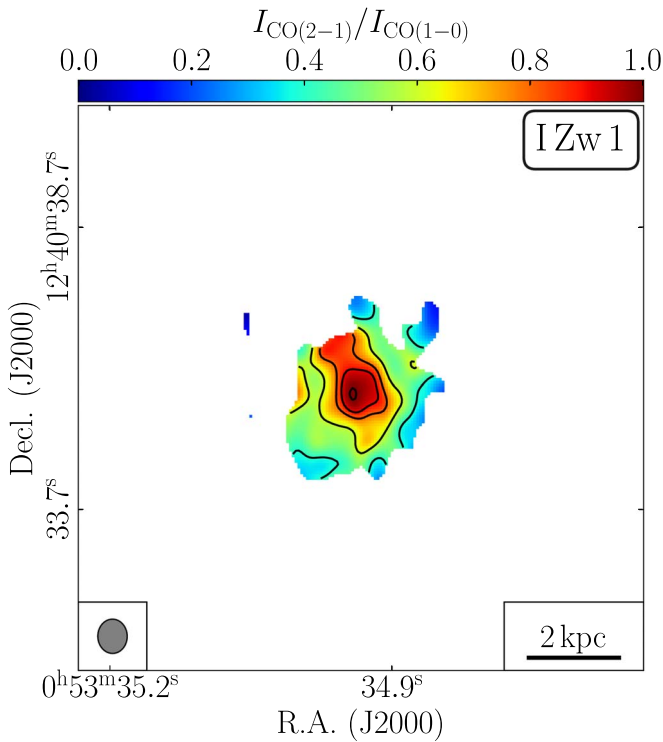
**Figure 6.** Surface brightness ratio between CO(2–1) and CO(1–0) in I Zw 1. The contour level corresponds to [0.4, 0.6, 0.8, 0.9, 1.0]. The ellipse in the bottom left represents the beam size of $0\rlap{.}{''}61 \times 0\rlap{.}{''}52$ for the CO(1–0) observation.

high-redshift galaxies (Carilli & Walter 2013; Daddi et al. 2015).

In the outer disk region, the emission-line ratio is relatively low ($\lesssim 0.6$). It is likely that at larger radii the molecular gas becomes subthermally excited (Husemann et al. 2017) or has a lower temperature (Braine & Combes 1992).

### 5.2. Star Formation Law of the Nuclear Region

We check the Kennicutt–Schmidt (KS) relation (Kennicutt 1998) in the nuclear region of I Zw 1 based on the CO(2–1) line and continuum maps and the new $\alpha_{CO}$ value of $\sim 1.5\,M_{\odot}(\text{K km s}^{-1}\,\text{pc}^2)^{-1}$ derived from our dynamical modeling fitting.

The ALMA continuum image reveals a 1.3 mm continuum flux density of $\sim 1.1$ mJy from the central $3\sigma$ contour region. Molina et al. (2023) decomposed the SED of I ZW 1. They estimated that the AGN contribution, including the nonthermal synchrotron emission extrapolated from the radio bands and the thermal free–free emission, contribute about 28% ($\sim 0.30$ mJy) of the ALMA continuum, and the remaining 72% is likely to be from the thermal dust heated by nuclear star formation. Based on this decomposition of the ALMA continuum, they calculated a nuclear SFR of $5.43\,M_{\odot}\,\text{yr}^{-1}$.

The AGN contribution to the millimeter dust continuum emission could also be estimated and removed based on the empirical luminosity relations. Kawamuro et al. (2022) present a relationship between the rest-frame 1.3 mm wave ($\nu L_{\nu,\text{mm}}$) and 2–10 keV X-ray luminosities ($L_{2-10\,\text{keV}}$) for AGNs (see Table 1 in Kawamuro et al. 2022). Based on this relation, and adopting the 2–10 keV luminosity of I ZW 1 from Piconcelli et al. (2005), we estimate an AGN contribution to the 1.3 mm continuum flux density of $0.35^{+0.65}_{-0.23}$ mJy. This flux density has

been corrected to the observing frame assuming a millimeter-wave spectral index of 0.5 ($S_{1.3\,\text{mm}} \propto \nu^{-0.5}$). This value is consistent with that derived from the synchrotron and free–free components in the SED decomposition, considering the large uncertainty of 0.45 dex of the $\nu L_{\nu,\text{mm}}$–$L_{2-10\,\text{keV}}$ relation. Therefore, we adopt the nuclear SFR of $5.43\,M_{\odot}\,\text{yr}^{-1}$ from Molina et al. (2023) in the analysis here.

The face-on size of the star-forming region is estimated by $A = S/\cos i$, where $S$ is the area within the $3\sigma$ contour region of the continuum map and $i$ is the inclination angle. Thus, the mean surface density of the SFR in the nuclear region can be estimated by $\Sigma_{\text{SFR}} = \text{SFR}/A$.

We then estimate the mean molecular gas surface density using the CO(2–1) flux in the aforementioned region. By assuming $R_{21}$ following the CO emission-line ratio map presented in Figure 6, we estimate the CO(1–0) emission-line flux in this region. Finally, we estimate the gas surface density with $\Sigma_{\text{mol}} = \alpha_{CO} \times L'_{CO(1-0)}/A$, where $\alpha_{CO} = 1.5\,M_{\odot}(\text{K km s}^{-1}\,\text{pc}^2)^{-1}$ is the CO-to-$H_2$ conversion factor and $L'_{CO(1-0)}$ is the CO(1–0) luminosity in the nuclear region. We also present an estimation of the molecular gas surface density by adopting an $\alpha_{CO}$ value of $4.3\,M_{\odot}(\text{K km s}^{-1}\,\text{pc}^2)^{-1}$, which is a typical value of a MW-like galaxy, for comparison (Bolatto et al. 2013).

We compare the derived surface densities of the SFR and of molecular gas mass in the plot of the KS relation in Figure 7. The mean SFR and molecular gas surface densities in the nuclear region (filled blue circle) of I Zw 1 are comparable to the typical values of starburst galaxies (open diamonds in Figure 7; García-Burillo et al. 2012; Kennicutt & De Los Reyes 2021), and larger than those of normal star-forming galaxies (open circles in Figure 7; Leroy et al. 2013; de los Reyes & Kennicutt 2019). We also investigate the surface densities of the SFR and molecular gas for the central peak (filled red circle), and find that this data point is located well within a starburst source region. The gas depletion timescale is derived using $\tau_{\text{dep}} = \Sigma_{\text{mol}}/\Sigma_{\text{SFR}}$. We found $\tau_{\text{dep}} \sim 300$ Myr, which is close to that of local starburst systems. We also present the gas surface densities adopting $\alpha_{CO} = 4.3$ $M_{\odot}(\text{K km s}^{-1}\,\text{pc}^2)^{-1}$ from Bolatto et al. (2013), which are shown as filled red and blue stars in Figure 7 and are located below the KS relation for starburst systems.

We find that this quasar host galaxy has enhanced star-forming activity in its central $\lesssim 500$ pc region. The starburst activity suggests that AGN feedback plays a minor role in stopping ongoing star formation, and a positive influence can also be plausible. Assuming a MW-like $\alpha_{CO}$ increases the molecular gas surface density significantly, while the data points are still close to a ULIRG-like KS relation, and are still well above the KS relation for local star-forming galaxies (Figure 7). Nuclear starbursts have also been found in other low-$z$ quasars (Cresci et al. 2004; Schweitzer et al. 2006; Romeo & Fathi 2016; Molina et al. 2023).

### 5.3. Does an AGN Perturb the Cold Molecular Gas?

We measure an intrinsically large velocity dispersion in the galactic nucleus from our kinematic analysis in Section 3.2, which is $3 \sim 4$ times higher than the values measured in the outer region with radii $> 0.8$ kpc. Such a large velocity dispersion indicates that the molecular gas in this central 1 kpc region has a large turbulent energy. There are several possible mechanisms that may contribute to this turbulent ISM.
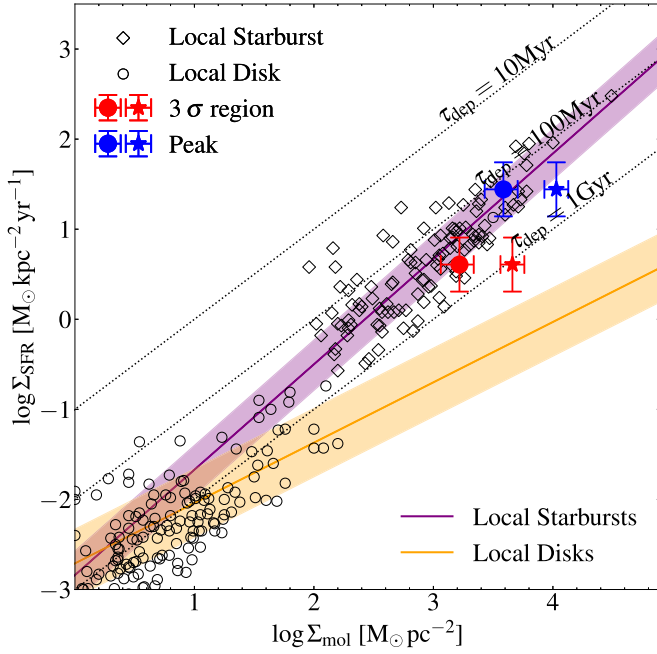
**Figure 7.** The surface density of molecular gas vs. surface density of the SFR in the nuclear of I Zw 1. The open markers represent star-forming galaxies (circles; de los Reyes & Kennicutt 2019) and starburst galaxies (diamonds; Kennicutt & De Los Reyes 2021) in the local universe. The orange and purple solid lines represent the KS law for local star-forming and starburst galaxies (de los Reyes & Kennicutt 2019; Kennicutt & De Los Reyes 2021), whose surrounding shaded region represents scatter on an order of ∼0.3 dex. The filled red point shows the mean surface density measured within the $3\sigma$ contour region of the continuum map (Figure 4), while the filled blue point gives the peak values of the molecular gas and SFR surface densities measured within the central beam. The filled stars represent the gas surface density if a MW-like $\alpha_{CO}$ is adopted. The dotted lines show the trends with gas depletion timescales $\tau_{dep} = 10$ Myr, 100 Myr, and 1 Gyr.

This large velocity dispersion might be related to the high gas surface density, since the ISM turbulent pressure ($P_{ISM}$) should be in equilibrium with the weight ($\mathcal{W}$) of the ISM (Sun et al. 2020; Ostriker & Kim 2022). The enormous energy released by a central AGN could also perturb the ISM. The central starburst may also enhance the gas velocity dispersion by means of stellar feedback. To check whether such large velocity dispersion originates from the AGN and stellar feedback, we try to identify whether there is an excess in the ISM turbulent pressure ($P_{ISM}$), comparing to the weight ($\mathcal{W}$) of the ISM. Any excess ISM turbulent pressure should represent the energy released by a central AGN or starburst.

The weight of the ISM can be expressed as follows (Ostriker & Kim 2022):

$$\mathcal{W} = \pi G \Sigma_g^2 / 2 + 4\pi \zeta_d G \Sigma_g \rho_{sd} h_g. \quad (7)$$

The first term is the weight due to the self-gravity of the ISM's disk (Spitzer 1942; Elmegreen 1989). Here the surface density of the ISM should have at least two components in principle, i.e., $\Sigma_g = \Sigma_{H_2} + \Sigma_{HI}$. However, we note that the atomic gas is negligible in the galaxy center. Therefore we replace $\Sigma_g$ with $\Sigma_{H_2}$ in the remaining context. The second term is the weight of the ISM due to external gravity, including the stellar component and dark matter halo. The numerical value of $\zeta$ depends on, but not sensitively to, the geometric distribution of the gas disk, and thus can be assumed as a constant of ∼a third (see Equation (6) of Ostriker et al. 2010), and $\rho_{sd}$ is the external density. In the galaxy center where the external

gravitational potential is dominated by the stellar bulge, $\rho_{sd}$ could be estimated using the bulge mass density of $\rho_b$. This term also accounts for the half-thickness of the gas disk, $h_g$, whose typical value is about $100-200$ pc (Wilson et al. 2019).

The ISM turbulent pressure at the midplane is defined by the difference in the total vertical momentum flux across the gas layer, and thus can be expressed as

$$P_{ISM} = \rho_{mid} \sigma_g^2 (1 + \alpha + \beta) = \frac{\Sigma_g}{2h_g} \sigma_g^2 (1 + \alpha + \beta), \quad (8)$$

where $\sigma_g$ is the velocity dispersion of molecular gas and can be measured from the CO emission line. The parameters $\alpha \approx 0.3$ and $\beta \approx 0.0$ are the factors accounting for vertical-magnetic and cosmic-ray pressures' contributions (Kim & Ostriker 2015; Wilson et al. 2019).

As was pointed out in Ostriker & Kim (2022), the vertical hydrostatic equilibrium dictates that the ISM weight $\mathcal{W}$ must be equal to the ISM turbulent pressure $P_{ISM}$:

$$\mathcal{W} = P_{ISM}. \quad (9)$$

We examine the relationship between the ISM turbulent pressure and the weight of the ISM in this quasar host galaxy, pixel-by-pixel. We estimate the pixel-wise velocity dispersion using the following methods. In the first step, we generate a moment 2 map by applying a blanking mask using the Python package maskmoment.[9] The mask was created by starting at $5\sigma$ peaks in the cube and expanding down to the surrounding $2\sigma$ contour. The final moment maps are referred to as "dilated-mask" moment maps in Bolatto et al. (2017). Such a dilated moment 2 map can simultaneously capture low-level signal and avoid noise, and can well reproduce the observed velocity dispersion. In the second step, we build a rotating disk model using $^{3D}$Barolo to simulate the velocity dispersion that is solely caused by the beam-smearing effect. The model has the same CO(2–1) line intensity and rotation velocity as that from the I Zw 1 CO(2–1) data (Section 3.2), but the velocity dispersion of the model is set to be zero. Then the model is convolved with the synthesized beam of the I Zw 1 CO(2–1) data. We generate a simulated velocity dispersion from this model with a $2\sigma$ cutoff threshold. This simulated velocity dispersion is then removed from the dilated moment 2 map in quadrature to generate the intrinsic $\sigma_g$ map (Levy et al. 2018).

Based on the line ratio map discussed in Section 5.1, we estimate the CO(1–0) line surface brightness assuming $R_{21} = 0.9$ at $R < 0.8$ kpc and $R_{21} = 0.62$ at $R > 0.8$ kpc (Shangguan et al. 2020a). We then estimate the molecular gas mass by adopting $\alpha_{CO} = 1.55\,M_\odot$(K km s$^{-1}$ pc$^2$)$^{-1}$ from the dynamical modeling as shown in Section 4.3. The $\rho_{sd}$ is estimated from dynamical modeling and follows Equation (5). We estimate these two pressures by assuming a constant gas disk scale height of $h_g = 150$ pc, which is a typical value of nearby ULIRG and starburst systems (Wilson et al. 2019; Molina et al. 2020). The relations between $P_{ISM}$ and $\mathcal{W}$ are plotted in Figure 8. We manually separate pixels into four groups depending on their radii: (i) $R < 0.4$ kpc, (ii) $0.4$ kpc $< R < 0.8$ kpc, (iii) $0.8$ kpc $< R < 2.1$ kpc, and (4) $R > 2.1$ kpc. We do not include data from group (iv) as the S/N of the CO(2–1) line in this region is too low. Also, we avoid presenting the data points from group (i) due to severe beam-smearing effect.
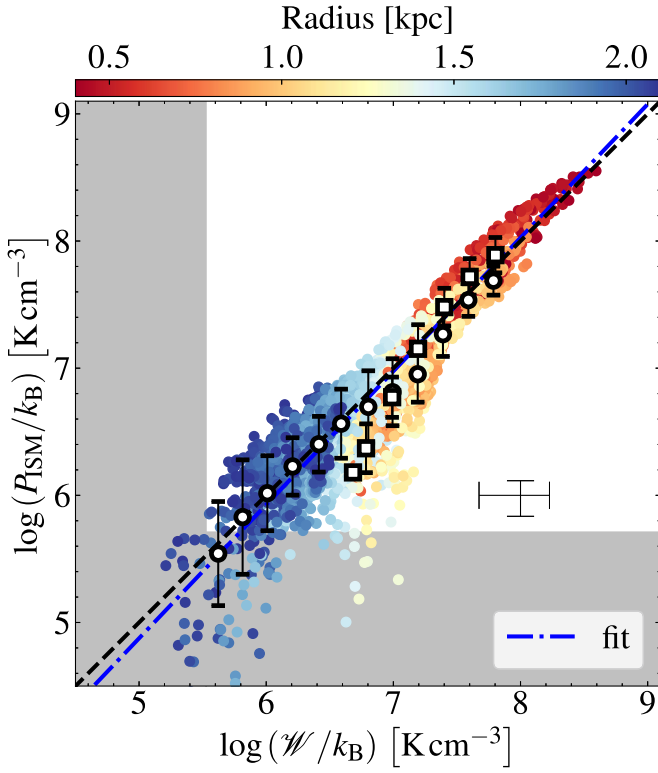
---

[9] https://github.com/tonywong94/maskmoment

**Figure 8.** The ISM turbulent pressure ($P_{ISM}$) as a function of ISM weight ($\mathcal{W}$). Data points represent pixels in the CO(2–1) map and are color-coded by the distance between pixels and the center of this galaxy, respectively. The open squares and circles represent the mean ISM turbulent pressure of each ISM weight bin, and denote data points in group (ii) and group (iii) as described in Section 5.3. The gray shaded region represents the lower limits of both pressures by considering the CO(2–1) detection limits. The dashed line denotes equality. The blue dashed–dotted lines represent the best-fitting power-law results. The typical uncertainty is plotted in the lower-right corner. This uncertainty is dominated by $\alpha_{CO}$, which is ~0.2 dex.

Figure 8 shows the relationship between $P_{ISM}$ and $\mathcal{W}$, spanning three orders of magnitude. The color of each data point represents the distance between each pixel and the galaxy center. In order to highlight the difference in groups (ii) and (iii), we calculate the mean and scatter trends for each group in 0.2 dex wide bins of fixed ISM weight.

We fit the relation between $P_{ISM}$ and $\mathcal{W}$ in logarithmic space using the Python package linmix (Kelly 2007). This yields the best-fitting power-law relations (blue dashed–dotted line in Figure 8):

$$\log\left(\frac{P_{ISM}}{k_B \, \mathrm{K \, cm^{-3}}}\right) = (-0.38^{+0.58}_{-0.56})$$
$$+ (1.05^{+0.08}_{-0.07}) \log\left(\frac{\mathcal{W}}{k_B \, \mathrm{K \, cm^{-3}}}\right).$$

The best-fitting result is consistent with the equality relation (black dashed line in Figure 8) considering the uncertainty. This result suggests that the origin of the high turbulent energy of the cold molecular gas (with $\sigma \sim 100 \, \mathrm{km \, s^{-1}}$) can be explained by the self-gravity of the galaxy alone.

### 5.4. The Lack of Negative AGN Feedback

The ALMA CO(2–1) image reveals that the molecular gas in the host galaxy of I Zw 1 is centrally concentrated with a high

surface density in the central 1 kpc region where intense star formation is taking place. This result is contradictory to the scenario in which AGN feedback can efficiently blow out the star-forming gas from the nuclear region and results in depletion of cold gas in the galaxy center (Rupke & Veilleux 2011; Ellison et al. 2021). In addition, there is no evidence of AGN-driven outflow in the nuclear region like other AGN host galaxies (e.g., Feruglio et al. 2020). As an alternative, we find an enhancement of gas velocity dispersion in the nuclear region, which indicates that the nuclear gas is dynamically hot compared with gas in the CND. However, we find that the ISM turbulent pressure is in equilibrium with the weight of the ISM, suggesting that the kinematics of molecular gas could be regulated by the host galaxy's self-gravity. A large velocity dispersion is naturally required to satisfy the hydrostatic equilibrium. There is no external energy budgets/pressure, e.g., from AGN feedback, that is expelling the cold gas from the galaxy center.

Thus far, Shangguan et al. (2020a) have reported that I Zw 1 is a CO luminous system and there is no evidence of galactic-scale molecular gas outflows. Lamperti et al. (2022) also report nondetection of molecular gas outflow from this object based on the ALMA high-resolution CO(2–1) data. Molina et al. (2021) found that the molecular gas in this galaxy is centrally concentrated, and rotating in a disk with negligible noncircular motions. Moreover, the continuum map reveals a centrally enhanced star formation (see also Molina et al. 2023), which also argues against the suppression of star formation from AGN feedback. From our kinematic and dynamical analysis, we find no evidence of AGN-driven outflow or an external gas energy budget. In addition, ionized gas components with high-velocity dispersions have been detected in some nearby quasar host galaxies from recent optical IFU data (Husemann et al. 2019; Singha et al. 2022). However, Molina et al. (2022) report that the kinetic energy of these gas components with high-velocity dispersions is only $\lesssim$0.1% of the AGN bolometric luminosities. This suggests that only a negligible percentage of the AGN power is coupled to the ISM. All these results suggest a lack of negative AGN feedback to the cold molecular gas and star formation in the quasar host galaxy.

### 6. Conclusions

We present a study of the CO(2–1) line emission in the nuclear region of I Zw 1 based on ALMA observations. A combination of all available data from the ALMA archive resolves the CO source on a 0″.36 scale with a spectral sensitivity of 0.28 mJy beam$^{-1}$ per channel. In the central 1 kpc region, molecular gas forms a high-density bar-like structure that has a different position angle compared to that of the main disk.

1. With $^{3D}$Barolo fitting, we obtain the intrinsic rotation velocity and velocity dispersion as a function of radius. This galaxy is a rotation-dominated system, similar to other star-forming galaxies in the local universe. The mean rotation velocity to dispersion ratio is about 9, which suggests that the molecular gas forms a cold disk. Meanwhile, the fitting results from the $^{3D}$Barolo model suggest an enhancement of velocity dispersion in the central subkiloparsec-scale region. We check the velocity field carefully and find that the pure beam-smearing effect cannot lead to such a large velocity dispersion. The

velocity dispersion of the molecular gas in the central region of the nuclear disk is intrinsically $\sim$3 times higher compared to that in the disk region.

2. The map of the emission-line ratio between the two CO emission lines represents a clear gradient of $R_{21}$ along the radius. The central value is close to the theoretical prediction under the assumption of thermalized, optically thick ISM conditions. In contrast, the main CND has relatively lower values.

3. We fit the rotation curve of the molecular gas disk and constrain the mass budget of the quasar host galaxy using a dynamical model. We take into account the constraints on gas distribution from the ALMA CO data and stellar morphology/mass from the HST imaging, and fit the CO-to-H$_2$ conversion factor. We find a best-fit $\alpha_{\rm CO} = 1.55^{+0.47}_{-0.49}\,M_\odot$ (K km s$^{-1}$ pc$^2$)$^{-1}$, which is between a ULIRG-like and MW-like $\alpha_{\rm CO}$ value $\alpha_{\rm CO,ULIRG} \approx 0.8\,M_\odot$(K km s$^{-1}$ pc$^2$)$^{-1}$, $\alpha_{\rm CO,MW} \approx 4.3\,M_\odot$(K km s$^{-1}$ pc$^2$)$^{-1}$.

4. We check the SFR and molecular gas surface densities in the central region, finding that the star formation activity follows the KS relation of local starburst galaxies, which suggests nuclear starburst activity.

5. By comparing the ISM turbulent pressure ($P_{\rm ISM}$) and the weight of the ISM ($\mathcal{W}$), we find these two parameters are almost equal to each other. The ISM turbulent pressure is in equilibrium with the galaxy's gravity, which suggests molecular gas in this galaxy is regulated by its self-gravity and there is no external energy budget that is expelling the cold gas. This result indicates that the central AGN, though luminous in the optical, is unlikely to be introducing extra pressure to the molecular gas in the nuclear region.

# Appendix A
## Testing the Gas Velocity Dispersion with Simulated Data

We build a mock observational data cube to test whether $^{\rm 3D}$Barolo is able to reproduce the intrinsic gas velocity dispersion with the reduction of the beam-smearing effect. We build a rotating disk model with the $^{\rm 3D}$Barolo galmod task. The model has the same CO(2–1) line intensity and rotation velocity as that from the I Zw 1 CO(2–1) data. However, the model has a constant velocity dispersion ($\sigma = 30$ km s$^{-1}$) along all radii. We then simulate the visibility data with CASA task simobserve, and image and clean this simulated visibility using the same procedure outlined in Section 2. We adjust the total integration time and ALMA configuration to obtain a similar S/N and angular resolution (the angular resolution of mock observation is $0\rlap{.}''33 \times 0\rlap{.}''30$). We then use $^{\rm 3D}$Barolo to fit the simulated data cube, and the results are shown in Figure 9. We can see that, if a gaseous rotating disk has a constant velocity dispersion with a value of 30 km s$^{-1}$ along all radii, the beam-smearing effect can boost the velocity dispersion by up to $\sim$60 km s$^{-1}$ in its center. With $^{\rm 3D}$Barolo analysis, although we cannot completely reduce the beam-smearing effect, the velocity dispersion has an error of $\lesssim$30% in the central region ($R \lesssim 1$ kpc). This result indicates that the centrally enhanced gas velocity dispersion ($\sigma \gtrsim 100$ km s$^{-1}$) that is found in the host galaxy of I Zw 1 may not be solely produced by the beam-smearing effect. Molecular gas in the center of this galaxy should have a very large velocity dispersion ($\sigma \gtrsim 100$ km s$^{-1}$) intrinsically. We also find that the velocity dispersion decreases at a large radius. This result is caused by the decreasing S/N of the simulated CO emission at the disk edge.
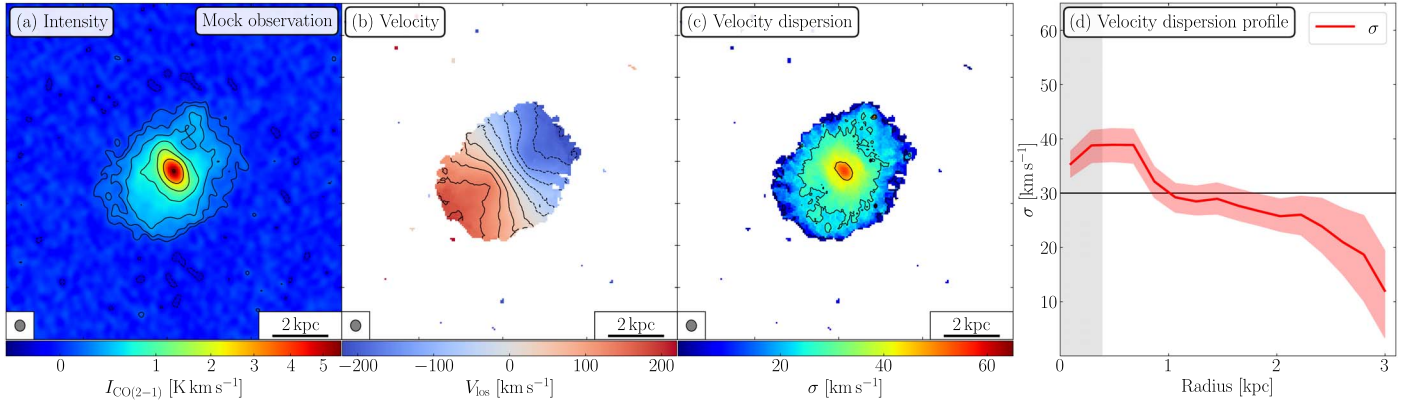
**Figure 9.** Panels (a), (b), and (c) show the velocity-integrated intensity map, the flux-weighted line-of-sight velocity map, and the velocity dispersion map of simulated data, respectively. The synthesized beam is shown as a gray ellipse in the bottom-left corner of each panel. The scale bar is shown in the bottom-right corner of each panel. Contours are the same as those in Figure 1. Panel (d) represents the velocity dispersion extracted from the mock observation through $^{3D}$Barolo. The red curve represents the best-fitting velocity dispersion from $^{3D}$Barolo, and the red shaded region represents the uncertainties. The horizontal line represents the input velocity dispersion of the simulated data. The synthesized beam ($0''33 \times 0''30$) is plotted in the lower-left corner of first three panels.

### Appendix B
### Dynamical Models with Different Prior Constraints

In this section, we try to fit the masses of the stellar bulge and stellar disk, and the CO-to-H$_2$ conversion factor by optimizing different prior constraints. In order to determine the degeneracy of the different components and different initial guesses of the parameters, we consider four main situations with a total of nine cases:

A. We set $\alpha_{CO}$ as a free parameter in the fitting and limit the stellar mass within the lower and upper limits of the stellar mass estimate (Zhao et al. 2021).
B. We set stellar mass as a free parameter and constrain the fitting range of $\alpha_{CO}$.
C. We try to fit $M_b$, $M_d$, and $\alpha_{CO}$ simultaneously with larger parameter spaces, thus those parameters are free.
D. We fit $M_b$, $M_d$, and $\alpha_{CO}$ without applying the asymmetric drift correction, to evaluate how significant the pressure gradient support against self-gravity is in this object.

In each case, $r_{e,b}$, $n$, $r_{e,d}$, $f_*$, and $c$ share the similar prior constraints (see Table 3). In case A.1, we assume Gaussian priors for $\log(M_b/M_\odot)$ with a centered value adopted from Zhao et al. (2021) and a standard deviation of 0.5. In case A.2, the adopted Gaussian prior is similar to that in case A.2, while the standard deviation is 3 times larger. In case A.3, we fix the mass of each stellar component and study the $\alpha_{CO}$ value. In case B.1, we assume a Gaussian prior for $\alpha_{CO}$ with a standard

deviation of 1 that is centered on the MW-like $\alpha_{CO}$ value, and we bound each stellar component mass within $\log(M_*/M_\odot) \in [8, 15]$. In case B.2, we fix the $\alpha_{CO}$ value to that of the MW and fit the stellar mass. In the case of C, we only bound the stellar mass and keep $\alpha_{CO}$ without any further prior assumption, e.g., a Gaussian distribution. In the case of D, we bound the stellar mass and $\alpha_{CO}$, but fit the rotation velocities without the asymmetric drift correction. All nine case conditions and their fitting results are listed in Table 4. We also provide the posterior distributions of eight cases in Figure 10.

We find that the $\alpha_{CO}$ value in case D is relatively smaller than those in cases A and C by a factor of $\sim$0.75, which indicates the effect of asymmetric drift correction. We also find that in case A.3, when we fix stellar mass, $\alpha_{CO}$ has an extremely low value that is immoderate. Further, in case B, if we adopt a MW-like value, the rotation velocity is dominated by molecular gas components. This case leaves very little room for the stellar bulge in the central region. The stellar bulge mass is less than 10 percent of the value derived from the stellar continuum image. This also results in a large stellar disk mass of $10^{11}$ $M_\odot$ to account for the rotation velocity in the outer part. This result requires a mass-to-light ratio that is different from the values adopted in Zhao et al. (2021), based on the $B$- and $I$-band colors. Thus, the MW $\alpha_{CO}$ value in case B is unlikely to be a good assumption. Cases A.1 and A.2, with a much lower $\alpha_{CO}$ value, present a more reasonable fitting for both the gas and stellar masses. As a consequence, we find that a ULIRG-like value for $\alpha_{CO}$ is reasonable in this quasar host galaxy.

**Table 4**
Constraints and Results of Dynamical Parameters

| Cases | Prior | | | Posterior | | |
|---|---|---|---|---|---|---|
| | $\log M_b$ ($M_\odot$) | $\log M_d$ ($M_\odot$) | $\alpha_{CO}$ [$M_\odot$ (K km s$^{-1}$ pc$^2$)$^{-1}$] | $\log M_b$ ($M_\odot$) | $\log M_d$ ($M_\odot$) | $\alpha_{CO}$ [$M_\odot$ (K km s$^{-1}$ pc$^2$)$^{-1}$] |
| A.1 | (10.5, 11.5) | (10.1, 11.1) | (0, 20) | $10.71^{+0.07}_{-0.08}$ | $10.60^{+0.33}_{-0.33}$ | $1.50^{+0.44}_{-0.47}$ |
| A.2 | (9.5, 12.5) | (9.1, 12.1) | (0, 20) | $10.70^{+0.08}_{-0.10}$ | $10.46^{+0.60}_{-0.84}$ | $1.55^{+0.47}_{-0.49}$ |
| A.3 | 10.96 | 10.64 | (0, 20) | 10.96 | 10.64 | $0.04^{+0.06}_{-0.03}$ |
| B.1 | (8, 15) | (8, 15) | $4.3 \pm 1.0$ | $10.53^{+0.14}_{-0.24}$ | $11.05^{+0.38}_{-1.37}$ | $2.28^{+0.49}_{-0.51}$ |
| B.2 | (8, 15) | (8, 15) | 4.34 | $9.73^{+0.24}_{-0.56}$ | $11.63^{+0.11}_{-0.14}$ | 4.34 |
| C | (8, 15) | (8, 15) | (0, 20) | $10.73^{+0.07}_{-0.09}$ | $9.97^{+0.90}_{-1.23}$ | $1.44^{+0.44}_{-0.46}$ |
| D.1 | (10.5, 11.5) | (10.1, 11.1) | (0, 20) | $10.72^{+0.07}_{-0.08}$ | $10.58^{+0.34}_{-0.33}$ | $1.21^{+0.40}_{-0.43}$ |
| D.2 | (9.5, 12.5) | (9.1, 12.1) | (0, 20) | $10.74^{+0.06}_{-0.07}$ | $10.17^{+0.67}_{-0.71}$ | $1.12^{+0.39}_{-0.43}$ |
| D.3 | (8, 15) | (8, 15) | (0, 20) | $10.74^{+0.06}_{-0.08}$ | $9.88^{+0.95}_{-1.20}$ | $1.13^{+0.43}_{-0.44}$ |

**Note.** Prior constraints and posterior results of fitting. The uniform prior limits of the parameters are denoted as "(lower, upper)." The Gaussian priors of the parameters are denoted as $\mu \pm \sigma$. The fixed prior parameters are denoted as an individual number. The other parameters, $r_{e,b}$, $n$, $r_{e,d}$, $f_*$, and $c$, have the same prior distribution with their values adjusted as in Section 4.3.
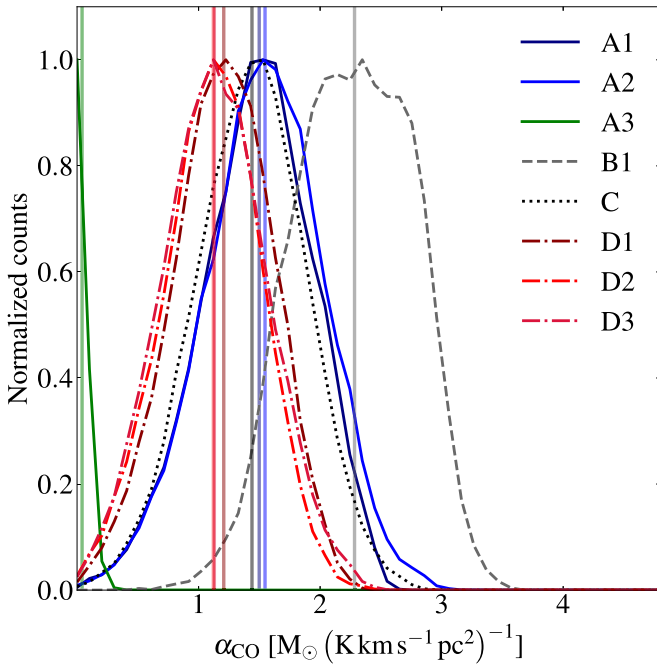


**Figure 10.** The posterior distribution function of $\alpha_{CO}$ of eight cases that have different prior constraints. The vertical lines represent the median values of the $\alpha_{CO}$ distribution, which are also shown in Table 4.

## ORCID iDs

Qinyue Fei ⬤ https://orcid.org/0000-0001-7232-5355
Ran Wang ⬤ https://orcid.org/0000-0003-4956-5742
Juan Molina ⬤ https://orcid.org/0000-0002-8136-8127
Jinyi Shangguan ⬤ https://orcid.org/0000-0002-4569-9009
Luis C. Ho ⬤ https://orcid.org/0000-0001-6947-5846
Franz E. Bauer ⬤ https://orcid.org/0000-0002-8686-8737
Ezequiel Treister ⬤ https://orcid.org/0000-0001-7568-6412

## References

Alonso-Herrero, A., Pereira-Santaella, M., García-Burillo, S., et al. 2018, ApJ, 859, 144
Astropy Collaboration, Robitaille, T. P., Tollerud, E. J., et al. 2013, A&A, 558, A33
Barvainis, R., Alloin, D., & Antonucci, R. 1989, ApJL, 337, L69
Barvainis, R., & Antonucci, R. 1989, ApJS, 70, 257
Behroozi, P. S., Conroy, C., & Wechsler, R. H. 2010, ApJ, 717, 379
Binney, J., & Tremaine, S. 2008, Galactic Dynamics (2nd ed.; Princeton, NJ: Princeton Univ. Press)
Bolatto, A. D., Wolfire, M., & Leroy, A. K. 2013, ARA&A, 51, 207
Bolatto, A. D., Wong, T., Utomo, D., et al. 2017, ApJ, 846, 159
Braine, J., & Combes, F. 1992, A&A, 264, 433
Bruhweiler, F., & Verner, E. 2008, ApJ, 675, 83
Burkert, A. 1995, ApJL, 447, L25
Burkert, A., Genzel, R., Bouché, N., et al. 2010, ApJ, 725, 2324
Carilli, C. L., & Walter, F. 2013, ARA&A, 51, 105
Chen, C.-T. J., Hickox, R. C., Alberts, S., et al. 2013, ApJ, 773, 3
Cicone, C., Maiolino, R., Sturm, E., et al. 2014, A&A, 562, A21
Cresci, G., Maiolino, R., Marconi, A., Mannucci, F., & Granato, G. L. 2004, A&A, 423, L13
Daddi, E., Dannerbauer, H., Liu, D., et al. 2015, A&A, 577, A46
de Blok, W. J. G., Walter, F., Brinks, E., et al. 2008, AJ, 136, 2648
de los Reyes, M. A. C., & Kennicutt, R. C. J. 2019, ApJ, 872, 16
den Brok, J. S., Chatzigiannakis, D., Bigiel, F., et al. 2021, MNRAS, 504, 3221
Di Teodoro, E. M., & Fraternali, F. 2015, MNRAS, 451, 3021
Ding, Y., Li, R., Ho, L. C., & Ricci, C. 2022, ApJ, 931, 77
Downes, D., & Solomon, P. M. 1998, ApJ, 507, 615
Dutton, A. A., & Macciò, A. V. 2014, MNRAS, 441, 3359
Eckart, A., van der Werf, P. P., Hofmann, R., & Harris, A. I. 1994, ApJ, 424, 627
Ellison, S. L., Wong, T., Sánchez, S. F., et al. 2021, MNRAS, 505, L46
Elmegreen, B. G. 1989, ApJ, 338, 178
Evans, A. S., Solomon, P. M., Tacconi, L. J., Vavilkin, T., & Downes, D. 2006, AJ, 132, 2398
Fabian, A. C. 2012, ARA&A, 50, 455
Ferrarese, L., & Merritt, D. 2000, ApJL, 539, L9
Feruglio, C., Maiolino, R., Piconcelli, E., et al. 2010, A&A, 518, L155
Feruglio, C., Fabbiano, G., Bischetti, M., et al. 2020, ApJ, 890, 29
Fiore, F., Feruglio, C., Shankar, F., et al. 2017, A&A, 601, A143
Fluetsch, A., Maiolino, R., Carniani, S., et al. 2019, MNRAS, 483, 4586
Foreman-Mackey, D., Hogg, D. W., Lang, D., & Goodman, J. 2013, PASP, 125, 306
Gallo, L. C., Boller, T., Brandt, W. N., Fabian, A. C., & Vaughan, S. 2004, A&A, 417, 29
García-Burillo, S., Usero, A., Alonso-Herrero, A., et al. 2012, A&A, 539, A8
Gebhardt, K., Bender, R., Bower, G., et al. 2000, ApJL, 539, L13
Haan, S., Schinnerer, E., Emsellem, E., et al. 2009, ApJ, 692, 1623
Huang, Y.-K., Hu, C., Zhao, Y.-L., et al. 2019, ApJ, 876, 102
Hubble, E. P. 1926, ApJ, 64, 321
Husemann, B., Davis, T. A., Jahnke, K., et al. 2017, MNRAS, 470, 1570
Husemann, B., Scharwächter, J., Davis, T. A., et al. 2019, A&A, 627, A53
Israel, F. P. 1997, A&A, 328, 471
Kawamuro, T., Ricci, C., Imanishi, M., et al. 2022, ApJ, 938, 87
Kelly, B. C. 2007, ApJ, 665, 1489
Kennicutt, R. C. J. 1998, ApJ, 498, 541

Kennicutt, R. C. J., & De Los Reyes, M. A. C. 2021, ApJ, 908, 61
Kewley, L. J., & Ellison, S. L. 2008, ApJ, 681, 1183
Kim, C.-G., & Ostriker, E. C. 2015, ApJ, 815, 67
King, A. R. 2010, MNRAS, 402, 1516
Kormendy, J., & Ho, L. C. 2013, ARA&A, 51, 511
Koss, M. J., Strittmatter, B., Lamperti, I., et al. 2021, ApJS, 252, 29
Krajnović, D., Cappellari, M., De Zeeuw, P. T., & Copin, Y. 2006, MNRAS, 366, 787
Lamperti, I., Pereira-Santaella, M., Perna, M., et al. 2022, A&A, 668, A45
Lang, P., Förster Schreiber, N. M., Genzel, R., et al. 2017, ApJ, 840, 92
Lanzuisi, G., Delvecchio, I., Berta, S., et al. 2017, A&A, 602, A123
Larson, K. L., Sanders, D. B., Barnes, J. E., et al. 2016, ApJ, 825, 128
Leroy, A. K., Bolatto, A., Gordon, K., et al. 2011, ApJ, 737, 12
Leroy, A. K., Walter, F., Sandstrom, K., et al. 2013, AJ, 146, 19
Levy, R. C., Bolatto, A. D., Teuben, P., et al. 2018, ApJ, 860, 92
Lombardi, M., Alves, J., & Lada, C. J. 2006, A&A, 454, 781
Lyu, J., Rieke, G. H., & Smith, P. S. 2019, ApJ, 886, 33
Magorrian, J., Tremaine, S., Richstone, D., et al. 1998, AJ, 115, 2285
McMullin, J. P., Waters, B., Schiebel, D., Young, W., & Golap, K. 2007, in ASP Conf. Ser. 376, Astronomical Data Analysis Software and Systems XVI, ed. R. A. Shaw, F. Hill, & D. J. Bell (San Francisco, CA: ASP), 127
Molina, J., Ho, L. C., Wang, R., et al. 2022, ApJ, 935, 72
Molina, J., Ho, L. C., Wang, R., et al. 2023, ApJ, 944, 30
Molina, J., Ibar, E., Godoy, N., et al. 2020, A&A, 643, A78
Molina, J., Wang, R., Shangguan, J., et al. 2021, ApJ, 908, 231
Morganti, R., Oosterloo, T., Oonk, J. B. R., Frieswijk, W., & Tadhunter, C. 2015, A&A, 580, A1
Mosenkov, A. V., Sotnikova, N. Y., Reshetnikov, V. P., Bizyaev, D. V., & Kautsch, S. J. 2015, MNRAS, 451, 2376
Mullaney, J. R., Daddi, E., Béthermin, M., et al. 2012, ApJL, 753, L30
Narayanan, D., Krumholz, M., Ostriker, E. C., & Hernquist, L. 2011, MNRAS, 418, 664
Navarro, J. F., Frenk, C. S., & White, S. D. M. 1996, ApJ, 462, 563
Noordermeer, E. 2008, MNRAS, 385, 1359
Osterbrock, D. E. 1977, ApJ, 215, 733
Ostriker, E. C., & Kim, C.-G. 2022, ApJ, 936, 137
Ostriker, E. C., McKee, C. F., & Leroy, A. K. 2010, ApJ, 721, 975
Papadopoulos, P. P., van der Werf, P. P., Xilouris, E. M., et al. 2012, MNRAS, 426, 2601
Perna, M., Arribas, S., Pereira Santaella, M., et al. 2021, A&A, 646, A101
Pettini, M., & Pagel, B. E. J. 2004, MNRAS, 348, L59
Phillips, M. M. 1976, ApJ, 208, 37
Piconcelli, E., Jimenez-Bailón, E., Guainazzi, M., et al. 2005, A&A, 432, 15

Planck Collaboration, Ade, P. A. R., Aghanim, N., et al. 2016, A&A, 594, A13
Prugniel, P., & Simien, F. 1997, A&A, 321, 111
Rogstad, D. H., Lockhart, I. A., & Wright, M. C. H. 1974, ApJ, 193, 309
Romeo, A. B., & Fathi, K. 2015, MNRAS, 451, 3107
Romeo, A. B., & Fathi, K. 2016, MNRAS, 460, 2360
Rosolowsky, E., Leroy, A. K., Usero, A., et al. 2015, AAS Meeting, 225, 141.25
Rupke, D. S. N., & Veilleux, S. 2011, ApJL, 729, L27
Saintonge, A., Catinella, B., Tacconi, L. J., et al. 2017, ApJS, 233, 22
Sanders, D. B., Scoville, N. Z., & Soifer, B. T. 1991, ApJ, 370, 158
Sandstrom, K. M., Leroy, A. K., Walter, F., et al. 2013, ApJ, 777, 5
Schawinski, K., Thomas, D., Sarzi, M., et al. 2007, MNRAS, 382, 1415
Schinnerer, E., Eckart, A., & Tacconi, L. J. 1998, ApJ, 500, 147
Schmidt, M., & Green, R. F. 1983, ApJ, 269, 352
Schweitzer, M., Lutz, D., Sturm, E., et al. 2006, ApJ, 649, 79
Sérsic, J. L. 1963, BAAA, 6, 41
Shangguan, J., Ho, L. C., Bauer, F. E., Wang, R., & Treister, E. 2020a, ApJS, 247, 15
Shangguan, J., Ho, L. C., Bauer, F. E., Wang, R., & Treister, E. 2020b, ApJ, 899, 112
Shangguan, J., Ho, L. C., & Xie, Y. 2018, ApJ, 854, 158
Silva, C. V., Costantini, E., Giustini, M., et al. 2018, MNRAS, 480, 2334
Singha, M., Husemann, B., Urrutia, T., et al. 2022, A&A, 659, A123
Solomon, P. M., Rivolo, A. R., Barrett, J., & Yahil, A. 1987, ApJ, 319, 730
Spitzer, L. 1942, ApJ, 95, 329
Staguhn, J. G., Schinnerer, E., Eckart, A., & Scharwächter, J. 2004, ApJ, 609, 85
Sturm, E., González-Alfonso, E., Veilleux, S., et al. 2011, ApJL, 733, L16
Sun, J., Leroy, A. K., Schinnerer, E., et al. 2020, ApJL, 901, L8
Tan, Q.-H., Gao, Y., Kohno, K., et al. 2019, ApJ, 887, 24
van der Walt, S., Colbert, S. C., & Varoquaux, G. 2011, CSE, 13, 22
Virtanen, P., Gommers, R., Oliphant, T. E., et al. 2020, NatMe, 17, 261
Vito, F., Maiolino, R., Santini, P., et al. 2014, MNRAS, 441, 1059
Walter, F., Brinks, E., de Blok, W. J. G., et al. 2008, AJ, 136, 2563
Wang, J., Koribalski, B. S., Serra, P., et al. 2016, MNRAS, 460, 2143
Wilson, C. D., Elmegreen, B. G., Bemis, A., & Brunetti, N. 2019, ApJ, 882, 5
Wolfire, M. G., Hollenbach, D., & McKee, C. F. 2010, ApJ, 716, 1191
Xia, X. Y., Gao, Y., Hao, C. N., et al. 2012, ApJ, 750, 92
Yajima, Y., Sorai, K., Miyamoto, Y., et al. 2021, PASJ, 73, 257
Zhao, Y., Ho, L. C., Shangguan, J., et al. 2021, ApJ, 911, 94
Zhuang, M.-Y., Ho, L. C., & Shangguan, J. 2021, ApJ, 906, 38